1
2
# Numerical Case Study of the Aerosol-Cloud-Interactions in Warm Boundary Layer Clouds over the Eastern North Atlantic with an Interactive Chemistry Module

6
7
8
9

Hsiang-He Lee[1], Xue Zheng[1], Shaoyue Qiu[1], and Yuan Wang[2]

11
12
[1]Atmospheric, Earth, and Energy Division, Lawrence Livermore National Laboratory, Livermore, CA, U.S.A.
[2]Department of Earth System Science, Stanford University, Stanford, CA, U.S.A.

16
17
18
19
20
21
22
23
24
25
26
27
28
29
30
31
32
33
34
35
36
37

*Corresponding author address: Dr. Hsiang-He Lee, 7000 East Avenue, Livermore, CA, 94550, U.S.A.

E-mail: lee1061@llnl.gov

41

42

43

# Abstract

The presence of warm boundary layer stratiform clouds over the Eastern North Atlantic (ENA) region is commonly influenced by the Azores High, especially during the summer season. To investigate comprehensive aerosol-cloud interactions, this study employs the Weather Research and Forecast model coupled with a chemistry component (WRF-Chem), incorporating aerosol chemical components that are relevant with formation of cloud condensation nuclei (CCN) and accounting for aerosol spatiotemporal variation. This study focuses on aerosol indirect effects, particularly long-range transport aerosols, in the ENA region under three different weather regimes: ridge with surface high-pressure system, post-trough with surface high-pressure system, and weak trough. The WRF-Chem simulations conducted at a near the Large-Eddy Simulation scale offer valuable insights into the model's performance, especially regarding its high spatial resolution in accurately capturing the liquid water path (LWP) and cloud fraction across various weather regimes. Our result shows that introducing five times more aerosols to either non-precipitating or precipitating clouds significantly increases ambient CCN numbers, resulting in varying degrees of higher LWP. The substantial aerosol-cloud interaction especially occurs in the precipitating clouds and demonstrates the LWP susceptibility to changes in CCN under different regimes. Conversely, non-rain clouds at the edges of a cloud system are prone to evaporation, exhibiting an aerosol drying effect. The aerosols released during this process transition back to the accumulation mode, facilitating future activation. This dynamic behavior is not adequately represented in prescribed-aerosol simulations.

# 1  Introduction

Low-level stratiform clouds are predominantly generated over oceanic regions and are categorized into three main types: warm boundary layer stratiform clouds located on the eastern side of oceanic subtropical highs, stratocumulus clouds that develop over warm western boundary currents during winter cold outbreaks, and Arctic stratus (Klein and Hartmann, 1993). Warm boundary layer stratocumulus clouds, on average, blanket around 20% of the Earth's surface annually (Wood, 2012; Warren et al., 1988). Their influence on the Earth's energy balance is substantial, primarily through their ability to reflect incoming solar radiation, resulting in significant shortwave cloud radiative effects leading to a pronounced negative net radiative effect (Chen et al., 2000; Stephens and Greenwald, 1991; Hartmann et al., 1992).

Research on aerosol-cloud interactions in warm boundary layer clouds has been ongoing since the 1970s. Twomey (1974) proposed that aerosols play an important role in influencing the Earth's energy budget by serving as cloud condensation nuclei (CCN). These CCN are crucial for cloud formation. A higher concentration of CCN results in the formation of clouds with a greater number of smaller-sized cloud droplets (Twomey, 1991). These smaller droplets enhance cloud albedo, known as the first indirect effect, and inhibit precipitation formation while prolonging cloud lifetime, known as the second indirect effect (Albrecht, 1989). In addition to these indirect effects, aerosol particles have direct, semi-direct, and indirect impacts on the atmosphere's energy budgets and surface, leading to changes in atmospheric stability (Lee et al., 2008). Until now, our understanding of aerosol-cloud interactions remains incomplete. In a recent review paper, Feingold et al. (2024) highlighted that the response of cloud amount (including liquid water content, spatial coverage, and cloud persistence) to aerosol perturbations is still unclear. Both positive and negative adjustments in liquid water path (LWP) and cloud fraction (CF) have been

88    observed. Increases in cloud amount (positive adjustments) are linked to rain suppression, whereas

89    enhanced evaporation of smaller droplets and entrainment feedback tend to decrease cloud amount

90    (negative adjustments).

91         This study focuses on warm boundary layer stratiform clouds located on the eastern side

92    of oceanic subtropical highs, specifically targeting the area over the Eastern North Atlantic (ENA)

93    region, where the U.S. Department of Energy (DOE) Atmospheric Radiation Measurement (ARM)

94    program developed a ground-based user facility in the Azores archipelago (Mather and Voyles,

95    2013). Long-term ground-based observations at the ARM ENA site, aircraft field campaigns near

96    the Azores islands, and satellite retrievals over the ENA region provide comprehensive datasets

97    for observational studies on aerosol-cloud interactions (Zheng et al., 2022; Zheng et al., 2023;

98    Ghate et al., 2023; Qiu et al., 2024).

99         The presence of stratocumulus clouds over the ENA region is commonly influenced by the

100   Azores High, also known as the Bermuda-Azores High (Rémillard and Tselioudis, 2015). This

101   semi-permanent high-pressure system typically develops over the subtropical North Atlantic

102   Ocean. The Azores High often brings stable and relatively dry conditions to the region, which can

103   contribute to the formation and maintenance of stratocumulus clouds. During the summer season,

104   the Bermuda-Azores High tends to strengthen and expand, leading to more persistent high-pressure

105   conditions and often warmer, drier weather in its vicinity. Although synoptic intrusions from high

106   latitudes are less frequent in the summer compared to the winter season (Wood et al., 2015), the

107   ENA region still experiences synoptic variability from weak troughs during the summer months

108   (Mechem et al., 2018; Zheng et al., 2024).

4

109    Leveraging the marine boundary layer cloud observations from the ARM ENA

110    observatory, this study aims to study aerosol indirect effects (AIE), especially long-range transport

111    aerosols, in the warm boundary layer clouds over the ENA region under three different synoptic

112    regimes: ridge with surface high-pressure system, post-trough with surface high-pressure system,

113    and weak trough (Mechem et al., 2018; Zheng et al., 2024). These regimes are chosen because,

114    during them, the ARM site experiences northerly wind conditions, minimizing the influence of the

115    island effect on the observations (Ghate and Cadeddu, 2019; Zheng and Miller, 2022).

116    Only a few numerical studies examined aerosol-cloud interactions in marine boundary

117    layer clouds over this region (Zhang et al., 2021; Wang et al., 2020; Kazemirad and Miller, 2020;

118    Christensen et al., 2024). Wang et al. (2020), for example, used the Weather Research and Forecast

119    (WRF) model with prescribed CCN profiles to simulate perturbed long-range transport aerosol

120    concentration for two different cases of marine boundary layer (MBL) clouds. They concluded

121    that when long-range transport aerosol plumes penetrate down into the drizzling cloud deck, the

122    simulations show an increase in marine cloud fractions with larger water content, supporting a

123    positive cloud amount adjustment to CCN perturbations. Christensen et al. (2024) utilized an

124    advanced WRF configuration integrated with a Lagrangian framework to assess the effects of

125    aerosols on developing cloud fields across 10 case study days during the ENA field campaign and

126    got the same conclusion. However, a limitation of these studies is that they do not account for

127    aerosol composition acting as CCN or the changes in aerosol populations following the cloud

128    evaporation process, even though aerosol wet removal is included in their simulations.

129    To further investigate the impacts of realistic aerosol chemical components and aerosol

130    spatiotemporal variation on the AIE, this study adopts the WRF model coupled with a chemistry

131    component (WRF-Chem) to examine the AIE in the ENA region across different synoptic regimes.

132   A brief description of observational data and the WRF-Chem model, as well as the configuration

133   and numerical experiments, are given in Section 2. Simulated results are discussed in Section 3,

134   including model evaluation, model sensitivity tests, and cloud susceptibilities. The discussion and

135   summary are provided in Section 4.

# 136   2  Methodology

## 137   2.1  Observational data

### 138   2.1.1  MERRA-2

139   The Modern-Era Retrospective analysis for Research and Applications, Version 2

140   (MERRA-2), represents the latest advancement in global atmospheric reanalysis during the

141   satellite era. Produced by NASA's Global Modeling and Assimilation Office (GMAO), it utilizes

142   the Goddard Earth Observing System Model (GEOS) version 5.12.4 (Molod et al., 2015). The

143   aerosol species are from the dataset, inst3_3d_aer_Nv, which is an instantaneous 3-dimensional 3-

144   hourly data collection in MERRA-2 (Modeling and Office, 2015). The dataset comprises

145   assimilations of aerosol mixing ratio parameters at a native resolution of 0.5° latitude x 0.625°

146   longitude across 72 model layers, encompassing dust, sea salt, sulfur dioxide ($SO_2$), sulfate ($SO_4$),

147   black carbon (BC), and organic carbon (OC). The data is provided every three hours, beginning

148   at 00:00 UTC. Based on Wang et al. (2020), we also adopt MERRA-2 to drive the WRF-Chem

149   initial and boundary conditions for this study (see Sect. 2.2.2 for details).

### 150   2.1.2  Geostationary satellite retrievals (Meteosat)

151   Cloud properties are derived from the Spinning Enhanced Visible and Infrared Imager

152   (SEVIRI) on Meteosat-10 and Meteosat-11, which offer a spatial resolution of 3 km at nadir and

153   a half-hourly temporal resolution over the ENA region. These SEVIRI cloud products are

154    generated using the Satellite ClOud and Radiation Property retrieval System (SatCORPS)

155    algorithms (Painemal et al., 2021). These methods, developed by the Clouds and Earth's Radiant

156    Energy System (CERES) project, are specifically tailored to support the ARM program at ARM

157    ground-based observation sites (Minnis et al., 2011; Minnis et al., 2021). Specifically, this study

158    adopts cloud fraction as the observational reference over the ENA region. The adopted data have

159    been specifically processed (e.g., solar zenith angle, cloud optical thickness, and cloud labels) and

160    averaged to 25 km × 25 km (Qiu et al., 2024).

### 2.1.3 Aircraft observation

162    The U.S. DOE ARM Aerosol and Cloud Experiments in the Eastern North Atlantic (ACE-

163    ENA) aircraft field campaign near the Azores islands provided extensive observations of the

164    vertical distributions of aerosol and cloud properties (Wang et al., 2022). Intensive operational

165    periods (IOPs) of the ACE-ENA took place in late June and July 2017, as well as January to

166    February 2018. During the 2017 summer IOP, the ARM Aerial Facility's (AAF) Gulfstream-159

167    (G-1) aircraft delivered precise measurements of aerosol size distribution, total aerosol number

168    concentration, and chemical constituents both below and above cloud layers. SO$_4$ and OC mass

169    concentrations were measured using the Aerodyne High-Resolution Time-of-Flight Aerosol Mass

170    Spectrometer (HR-ToF-AMS), while refractory BC was measured by the Single Particle Soot

171    Photometer (SP2). Detailed information about each instrument is available on the ARM website

172    (https://www.arm.gov/research/campaigns/aaf2017ace-ena). In this study, aircraft measurements

173    of SO$_4$, OC, and BC from 19 July 2017, are utilized to assess the simulated aerosol vertical profile.

174    However, uncertainties arising from the measurements and spatiotemporal sampling strategies

175    may hinder direct comparisons of absolute values between the observations and modeled results.

7

### 2.1.4 ARM ground-based observations

176

177       The DOE ARM ground-based instruments deployed on Graciosa Island in the Azores

178 archipelago provide comprehensive measurement of aerosols, clouds, radiation, atmospheric

179 boundary layer, and other atmospheric properties. In this study, liquid water path (LWP) is

180 retrieved from the brightness temperature measured by the microwave radiometer (MWR) at 23.8

181 and 31.4 GHz (Liljegren et al., 2001) and used for model evaluation. The temperature and moisture

182 profiles are from the interpolated sonde data, derived from the radiosonde measurement.

## 2.2 The model

183

### 2.2.1 WRF-Chem

184

185       The Weather Research and Forecasting (WRF) model version 4.4.2 (Skamarock et al.,

186 2021) coupled with a chemistry component (WRF-Chem) (Grell et al., 2005) is used in this study.

187 The standard WRF-Chem permits the simulation of the combined direct, indirect, and semi-direct

188 effects of aerosols (Grell et al., 2005; Fast et al., 2006; Chapman et al., 2009). WRF-Chem version

189 4.4.2 has sophisticated packages to represent chemistry processes (i.e., gas-phase reaction, gas-to-

190 particle conversion, coagulation, etc.) and aerosol size and composition (Binkowski and Shankar,

191 1995). In this study, the Regional Acid Deposition Model version 2 (RADM2) photochemical

192 mechanism (Stockwell et al., 1997) is integrated alongside the Modal Aerosol Dynamics Model

193 for Europe (MADE) and the Secondary Organic Aerosol Model (SORGAM) (Ackermann et al.,

194 1998; Schell et al., 2001) to simulate atmospheric chemistry and the evolution of anthropogenic

195 aerosols. MADE/SORGAM adopts a modal approach to represent the aerosol size distribution,

196 predicting mass and number concentrations across three aerosol modes (Aiken, accumulation, and

197 coarse). MADE/SORGAM has inorganic, organic, and secondary organic aerosols and contain

198 aerosol formation processes including nucleation, condensation, and coagulation. WRF-Chem

199    tracks the number of particles and the mass of chemical compounds (e.g., $SO_4^{2-}$, $NH_4^+$, $NO_3^-$, $Na^+$,

200    $Cl^-$ etc.) in each aerosol mode, including both interstitial aerosols and aerosols present in liquid

201    water (the sum of cloud and rain), as prognostic variables.

202        The size, composition, and mixing state of aerosols significantly influence their capability

203    to activate as CCN (Zaveri et al., 2010). A physically based aerosol activation parameterization

204    scheme has been developed for climate models to simulate CCN concentration accurately and

205    efficiently (Abdul-Razzak and Ghan, 2000). This aerosol activation parameterization was initially

206    designed for a single aerosol type with a lognormal size distribution. Then, they expanded this

207    parameterization to accommodate multiple externally mixed lognormal modes, with each mode

208    consisting of both soluble and insoluble materials internally mixed. However, WRF-Chem

209    (MADE/SORGAM) chemistry package adopts this global internal mixing assumption, where all

210    particles within a log-normal mode within the same grid cell are instantly combined, resulting in

211    the same chemical composition. This instantaneous internal mixing assumption modifies the

212    optical and chemical characteristics of particles in WRF-Chem simulations, potentially impacting

213    aerosol-cloud interactions, such as aerosol activation as CCN (Zhang et al., 2014).

214    ### 2.2.2  The configuration

215        Our focus in this study is to examine aerosol-cloud interactions close to the scale of large-

216    eddy simulation (LES) over the ARM ENA site. We use WRF-Chem with a full chemistry

217    package involving sophisticated gaseous and aqueous chemical processing calculations and dry

218    and wet depositions. The numerical simulations are employed with 4 domains with 4 horizontal

219    resolutions of 5 km, 1.67 km, 0.56 km, and 0.19 km, respectively (Fig. 1), with one-way nesting.

220    Seventy-five vertically staggered layers are stretched to have a higher resolution near the surface

221    based on a terrain-following pressure coordinate system. With this setup, the model has roughly

222  24 model layers in the boundary layer (~2000 m). The time step is 30 and 10 seconds for advection

223  and physics calculation for the domains 1 and 2, respectively. The nesting inner domains 3 and 4

224  have the time step of 3 seconds and 1 second, respectively. The physics schemes adopted in the

225  simulations are listed in Table 1. The initial and boundary meteorological conditions are taken

226  from ERA5, developed by the Copernicus Climate Change Service (C3S) at ECMWF (European

227  Centre for Medium-Range Weather), stands as the fifth generation of ECMWF atmospheric

228  reanalysis, spanning from January 1940 to the present day (Hersbach et al., 2023). This

229  comprehensive dataset offers hourly estimates of numerous atmospheric, land, and oceanic climate

230  variables, covering the entirety of Earth on a 31km grid. The atmospheric component is resolved

231  using 137 levels, spanning from the surface up to 80 km in height.

232  The computational expense of conducting a 4-domain WRF-Chem simulation, particularly

233  with LES resolution, is exceedingly high. To mitigate this, we execute WRF solely for the two

234  outer domains (d01 and d02), leveraging the WRF downscaling module (ndown) (Skamarock et

235  al., 2008) to generate meteorological initial and boundary conditions for domain 3. As a result,

236  we only need to perform WRF-Chem simulations for the two inner domains (d03 and d04), leading

237  to an almost 50% reduction in total computational costs (compared to the original 4-domain run,

238  which had a throughput of 4 hours per day using 1080 cores). It is important to note that a high

239  temporal frequency for domain 3 boundary conditions is essential due to its fine horizontal

240  resolution (0.56 km). In this context, we update the boundary condition every 5 minutes for

241  domain 3.

242  To enhance the realism of aerosol mass simulation in remote marine regions, such as the

243  ENA site, we account for major aerosol species (BC, OC, and $SO_4$), as well as $SO_2$, from MERRA-

244  2 into the boundary conditions of the domain 3. Aerosols in the initial condition are introduced

10

245 into the restart file (wrfrst) following a one-hour initial run, rather than in the initial condition file

246 (wrfinput), to address certain numerical challenges. According to the emission setup for

247 MADE/SORGAM, we assume that the Aiken mode and the accumulation mode account for 20%

248 and 80% of the aerosol mass (BC and OC), respectively (Tuccella et al., 2012). Conversely, for

249 $SO_4$, 80% is allocated to the Aiken mode and 20% to the accumulation mode, reflecting the faster

250 growth rate of $SO_4$ and a longer duration of growth from the domain 3 boundary. Because

251 MERRA-2 only provides aerosol mass, the aerosol number concentrations for different aerosol

252 species are estimated with the density assumption of BC (1.7 g cm$^{-3}$), OC (1.0 g cm$^{-3}$) and $SO_4$

253 (1.77 g cm$^{-3}$) based on Liu et al. (2012).

254 It is common to consider that the ENA region is an unpolluted area because it is far away

255 from the anthropogenic pollution sources. Besides long-range transport aerosols, two local aerosol

256 sources, dimethyl sulfide (DMS) and sea salts, are also important for the aerosol budget. Kazil et

257 al. (2011) pointed that the observed DMS flux from the ocean in the VOCALS-REx field campaign

258 over the Southeast Pacific can support a nucleation source of aerosol. DMS oxidation by nitrate

259 ($NO_3$) produces $SO_2$ and then increases $SO_4$ concentration (Toon et al., 1987). Since we adapted

260 $SO_2$ and $SO_4$ concentration from MERRA-2 in the initial and boundary conditions, we did not

261 double count DMS emissions in our simulations. As a result, chemical species emissions, except

262 for sea salt, are excluded from the simulations. The emission of sea salt particles is parameterized

263 using the method outlined by Clarke et al. (2006) in WRF-Chem. We adjust the parameter factor

264 for the sea salt emission to three times higher than the original estimate to achieve better agreement

265 with the sea salt aerosol variation in MERRA-2 reanalysis.

## 2.3 Study cases and numerical experiment design

266

267     We select three specific study cases to assess the impact of long-range transport aerosols on

268     warm boundary layer clouds, with each case representing a typical meteorological regime observed

269     over the ENA site.  The first case, dated 1 July 2016, exhibits the formation of overcast

270     stratocumulus clouds (Fig. 2a) within a meteorological regime characterized by a ridge system in

271     the free troposphere and a high-pressure system near the surface (Fig. 2d).  Predominant

272     northwesterly and northerly winds in the area of the ARM ENA site coincide with the presence of

273     long-range transport aerosols, commonly found along the periphery of the high surface pressure

274     system (Logan et al., 2014; Gallo et al., 2023).

275     The second case on 19 July 2017 is a stratocumulus cloud case (Fig. 2b) within a post-

276     trough regime featuring a high surface pressure under the influence of a trough system (Fig. 2e).

277     Following the trough passage, robust northwesterly winds facilitated the influx of long-range

278     transport aerosols into the region, which then shifted to northerly winds as the trough moved away.

279     Because the ACE-ENA aircraft field campaign ran on this time, more aerosol observational data

280     can be used to evaluate the model performance for this case.

281     Finally, the third case, dated 23 August 2019, occurred during a period of weak trough

282     activity (Fig. 2f).  Here, we noted the presence of broken, thicker clouds, often accompanied by

283     deeper cloud formations (Fig. 2c).  Long-range transport aerosols were again observed, primarily

284     carried by northwesterly and northerly winds, albeit with weaker surface wind speeds compared

285     to the preceding two cases.

286     All simulations start at 12 UTC on the preceding day of the study case, spanning a duration

287     of 36 hours, with the initial 12 hours dedicated to spin-up.  Again, aerosols in the initial condition

12

288  are introduced into the restart file after one-hour initial run (i.e., 13 UTC). The three

289  aforementioned cases, labeled as control cases (20160701_control, 20170719_control, and

290  20190823_control), are utilized to examine the behavior of warm boundary layer clouds under

291  diverse meteorological conditions. Additionally, we formulated three perturbed cases

292  (20160701_perturbed, 20170719_perturbed, and 20190823_perturbed) by amplifying aerosol

293  concentrations in both initial and boundary conditions, as well as sea salt emissions, by a factor of

294  five relative to each control case. These control cases represent clean conditions, with near-surface

295  CCN concentrations below 100 cm$^{-3}$ at the ARM ENA site. A comparison between the control

296  and perturbed cases elucidates the sensitivity of warm boundary layer clouds to aerosol

297  enhancements under varying meteorological conditions, thereby contributing to a deeper

298  understanding of cloud microphysics processes under varying atmospheric dynamics.

299  # 3  Results

300  ## 3.1  Model evaluation

301  ### 3.1.1  Meteorological conditions

302  Figures 2g, 2h, and 2i display the model-simulated liquid water path (LWP) in the control

303  runs over the domain 3 and 4. The simulations with fine spatial resolution effectively capture

304  synoptic frontal systems and cloud features, particularly when compared to the cloud images from

305  the Meteosat satellite (Figs. 2a, 2b, and 2c). Thin, uniform stratocumulus clouds on 1 July 2016

306  are simulated in 20160701_control, while the solid stratocumulus and frontal system on 19 July

307  2017 are also well captured in 20170719_control. Broken stratocumulus clouds on 23 August

308  2019 are reproduced in the simulation of 20190823_control.

309  The control runs serve as a basis for comparing the boundary layer structure against the

310  interpolated soundings obtained from the ARM ENA site. Figures 3 depict the comparison,

311   showing the simulated air temperature aligning closely with the observed values. However, on 1

312   July 2016, the model (20160701_control) displays a warm bias in capturing the temperature

313   inversion (Figs. 3a and 3b), with the simulated inversion layer situated approximately 200-300 m

314   lower than observed. Relative humidity has consistent performance and shows in Figs. S1a and

315   S1b. While the model indicates high relative humidity (> 90%) within 1000 m, observations show

316   this extending up to ~1200 m.

317   Moving to 19 July 2017, the model (20170719_control) successfully represents the diurnal

318   cycle of temperature vertical gradient within 1000 m height. However, compared to observations,

319   the model does not catch the inversion at 1500 m height and shows a warm bias in the model's

320   simulated temperature (Figs. 3c and 3d). The model simulation also tends to depict drier

321   conditions in the evening compared to the observation (Figs. S1c and S1d).

322   On 23 August 2019, characterized by a weak trough regime and higher boundary layer

323   height, the simulation of 20190823_control accurately captures warm and moist air advection in

324   the morning but struggles to maintain fidelity in the late afternoon. Notably, the lower troposphere

325   becomes excessively warm and dry after 18 UTC compared to observations (Figs. 3e, 3f, S1e, and

326   S1f).

327   In general, all simulations effectively capture large-scale conditions and cloud features

328   (Fig. 2) across different synoptic regimes but do not accurately represent temperature inversions

329   and air advection patterns. Discrepancies are noted in the simulated boundary layer height, which

330   is lower and the inversion is weaker than actual observations. Furthermore, the discrepancies tend

331   to increase in the later stage of simulation.

### 3.1.2 Aerosol evolution

332

333     As mentioned in Section 2.2.2, we incorporate major aerosol species (BC, OC, and $SO_4$),

334     from MERRA-2 into the domain 3 initial (in the restart file at 13 UTC) and boundary conditions

335     to enhance the realism of aerosol simulation. Figure 4 shows time-series $SO_4$ vertical profiles

336     from both MERRA-2 and WRF-Chem for three study cases. Here, we demonstrate the time

337     evolution of $SO_4$ because $SO_4$ is the main aerosol component among the three introduced aerosol

338     species, about 60~80% of total aerosol mass, in the initial conditions.

339     Compared to the MERRA-2 data, 20160701_control well captures the long-range transport

340     $SO_4$ between 1000 m and 2000 m, which is above the cloud deck, on 1 July 2016 (Figs. 4a and 4b).

341     The observed high BC and OC are also concentrated in this layer (Figs. S2a and S3a), as well as

342     simulated ones (Figs. S2b and S3b). Figure 4c and 4e show two MERRA-2 time-series vertical

343     distributions of $SO_4$ on 19 July 2017 and 23 August 2019, both showing low-altitude (below 1500

344     m) aerosol plumes. On 19 July 2017, the concentrations of BC and OC showed two peaks – one

345     near the surface and another above 1500 m in the free troposphere (Figs. S2c and S3c). This

346     pattern indicates the presence of a biomass-burning signature in the plume on that day (Wang et

347     al., 2020). While the simulation of 20170719_control did not capture the near surface BC, OC,

348     and $SO_4$ concentration after 12 UTC on 19 July 2017 (Figs. S2d, S3d, and 4d). It is because in the

349     case of the post-tough regime, the wind direction changes from northwesterly to northerly winds

350     when the trough moved away, the aerosol plume in the domain 3 did not propagate into the domain

351     4 when the wind direction change (figure not shown). However, the simulation of

352     20170719_control still captures the BC and OC plumes in the free troposphere (above 2000 m

353     height) (Figs. S2d and S3d).

15

354    Aircraft observations during the ACE-ENA provide more accurate depictions of aerosol

355    vertical distribution and aerosol layer heights, with differentiation of aerosol type. Figure 5a shows

356    the vertical distribution of aerosol mass concentrations averaged over the flights on 19 July 2017.

357    BC, OC and $SO_4$ all increase with height above clouds (~1000 m), indicating downward

358    propagation of aerosol plumes and possible interaction with MBL clouds (600 – 1000 m). Here,

359    we also see that high $SO_4$ in the free troposphere, same as the data in MERRA-2, but the model

360    underestimates the OC concentration in the free troposphere. On the other hand, within the MBL,

361    there is a much higher concentration of $SO_4$ in the MBL than those of BC and OC in the

362    observations. This phenomenon is also captured by the WRF-Chem simulation (Fig. 5b), but the

363    model did not capture the magnitude of $SO_4$ concentration.

364    Similarly, for the case of 23 August 2019, within the low boundary layer, there is a much

365    higher concentration of $SO_4$ in the low boundary layer (Fig. 4e). After 12 UTC on 23 August

366    2019, BC and OC show both high-altitude plumes and low-altitude plumes approaching into the

367    domain, which indicate potentially two different aerosol sources (Figs. S2e and S3e). Again, while

368    the simulation of 20190823_control well captures the time evolution of aerosol plume, the

369    boundary of high-altitude plumes and low-altitude plumes appears 300 m lower in the simulations

370    (~600 m in altitude; Figs. S2f and S3f) compared to the observations (~900 m in altitude).

371    Sea salts serve as an important source of CCN over the ocean, particularly in unpolluted

372    conditions. However, due to their larger particle size, sea salt particles tend to accumulate near

373    the ocean surface and are swiftly removed by dry deposition and sedimentation processes (Chin et

374    al., 2002). As discussed in Section 2.2, we adjusted the parameter factor to three times its original

375    value to better align with the MERRA-2 dataset. The simulation of 20160701_control (Figs. S4a

376    and S4b) accurately reproduces sea salt concentrations, both in magnitude and vertical distribution,

377    consistent with observations, same as the case of 20170719 (Figs. S4c and S4d). Nevertheless,

378    the model encounters difficulties in simulating sea salt concentrations for the case of 23 August

379    2019 (Figs. S4e and S4f), corresponding to a weak-trough system (Fig. 2c). Sea salt emissions in

380    WRF-Chem are driven by surface wind speed; however, the simulated surface wind speed matches

381    well with ERA-5 (Fig. S5). Hence, underestimated sea salt concentrations may stem from

382    inadequacies in emission parameterization, which is excessively determined by the surface wind

383    speed (Gong, 2003).

384    ### 3.1.3  Cloud properties

385        In Fig. 6, we observe a comparison between the simulated results and observations of LWP

386    and CF at different spatial scales (4 km- and domain-average, respectively) to leverage the

387    spatiotemporal advantages offered by both sets of observations. The ARM ground-based

388    instrument recorded an LWP of over 400 g m$^{-2}$ during the nighttime with drizzles reaching to the

389    surface on 1 July 2016 (Fig. 6a). As the sunrise (around 6 UTC), the LWP decreases to a range

390    about 100 g m$^{-2}$, and then increases again to 600 g m$^{-2}$ after 22 UTC.

391        To compare with the ARM ground-based observations, the WRF-Chem simulated result is

392    averaged over $20 \times 20$ grids centered on the Azores, which corresponds to an approximate

393    resolution of 4 km (Fig. 6a). Overall, the model generates a thin cloud layer with an

394    underestimated LWP during the nighttime, capturing only 10-20% of the observed LWP. The

395    simulated clouds are more consistent with the observations during the daytime. However, it is

396    important to note that the LWP retrieved by MWR experiences significant uncertainties during

397    drizzling or precipitating conditions. This is primarily due to the scattering effects of large

398    raindrops and raindrops accumulating on the instrument's radome, which can result in an

399    overestimation of LWP (Tian et al., 2019; Cadeddu et al., 2020).

400     Figure 6b depicts the comparison of CF between observations and WRF-Chem. The CF

401     values obtained from Meteosat are close to 1, indicating a solid cloud field. In contrast, the CF

402     simulated by WRF-Chem range between 0.5 and 0.9 on a domain-averaged scale. Similar to the

403     LWP results, the simulated CFs from WRF-Chem exhibit a diurnal cycle, with higher values

404     during the nighttime and lower values during the daytime. Due to the thinner clouds simulated in

405     WRF-Chem based on LWP, the modeled CF is 40-60% lower than the observation in the

406     afternoon, indicating that clouds dissipate more quickly in the model.

407     Compared to a ridge system like the case of 20160701, the WRF-Chem model is harder to

408     capture warm boundary layer clouds under a regime characterized by a post-trough system (like

409     the case of 20170719) or a weak trough system (like the case of 20190823). Compared to the

410     observations, the simulated LWP in 20170719_control is about 30% of the observed value (Fig.

411     6c. In contrast, the simulated CF performs better, reaching about 75% of the observed value (Fig.

412     6d). The discrepancy between the modeled results and observations may arise from delayed

413     moisture transfer from the outer domain or insufficient vertical resolution. In this instance, the

414     cloud systems move quickly under the post-trough weather regime. A 5-minute moisture input

415     from the boundary condition using WRF downscaling (ndown) may not be sufficient to transport

416     moisture into the inner domain, making it difficult for the model to develop thicker marine

417     stratocumulus clouds, especially for such high spacing resolution. On the other hand, in another

418     ongoing project, we have observed that increasing the vertical layers to 99 levels significantly

419     enhances the simulated cloud amount (figure not shown). Another possible reason is that the 6th

420     Order Horizontal Diffusion used in the study (diff_6th_opt = 2) is easy to break down the marine

421     stratiform clouds, especially in the high spacing resolution (Knievel et al., 2007). It is worth to

422     mention that Christensen et al. (2024) conducted sensitivity tests using various shallow cumulus

423    and microphysics schemes, and the different combinations of these schemes had a substantial

424    impact on the simulated cloud amount as well.

425        Moving to the case of 20190823, overall, compared to the observations, the model captures

426    LWP and CF slightly better, especially in the domain-averaged scale (Figs. 6e and 6f). Based on

427    the LWP observed from ARM, there are two systems passing in the area, one between 7 UTC to

428    14 UTC and the other between 18 UTC to 24 UTC on 23 August 2019. The simulation of

429    20190823_control captures the first system, but a little bit underestimates LWP; however, the

430    model misses the second system. The model simulated CFs also match well with Meteosat (Fig.

431    6f). Only after 18 UTC, the model misses catching the second system. The CFs drops 50 – 70 %

432    compared to the observations.

433        The underestimation of the cloud layer from the model simulations results in insufficient

434    longwave cooling at the cloud top, which may contribute to a weaker boundary layer inversion

435    and a shallower boundary layer depth identified in the previous section (negative feedback) (Zheng

436    et al., 2021).

437    ## 3.2  Aerosol composition and activation

438        The advantage of utilizing WRF-Chem to investigate aerosol-cloud interactions stems from

439    its capability to simulate the spatiotemporal distribution of CCN. This modeling is based on

440    various aerosol components and their sizes, as well as their dynamic responses to wet removal

441    processes associated with clouds and precipitation. In traditional simulations that rely on fixed or

442    prescribed aerosol distributions, accurately representing these factors can be particularly

443    challenging. WRF-Chem, however, allows for a more nuanced understanding by dynamically

444    modeling how aerosol populations evolve over time, especially after cloud evaporation processes.

445    During evaporation, the reduction in cloud water can lead to a re-entrainment of aerosols back into

446    the atmosphere, altering their concentration and properties.  This change can affect subsequent

447    cloud formation and precipitation patterns, highlighting the importance of capturing these

448    interactions for reliable predictions.

449        In this section, we concentrate on aerosol activation, considering its size and chemical

450    composition across three different cases.  The following section will discuss the aerosol indirect

451    effect and how changes in cloud properties feedback into the aerosol population and its activation

452    capability.

453        In Fig. 7a, the blue solid line and blue dashed line represent the vertical profiles of total

454    aerosol number concentration (including Aiken mode and accumulation mode) and aerosol number

455    concentration of the Aiken mode, respectively.  These profiles are averaged over the domain 4 on

456    1 July 2016.  The environment shown in the figure is characterized by its cleanliness, with a total

457    aerosol number concentration below the cloud top measuring less than 300 cm$^{-3}$.  In the

458    20160701_control simulation, the total aerosol number is low, and approximately 70% of the total

459    aerosol numbers belong to the Aiken mode.  According to the study conducted by Mccoy et al.

460    (2024), which utilized aerosol number concentration measurements from ARM airborne

461    observations on 15 July 2017, it was found that the ratio of the Aiken mode to the total aerosol

462    number was approximately 50-60% within an altitude of 1000 m.  Compared to this observational

463    analysis, our simulations generate an overabundance of small-sized aerosols, which result in a low

464    concentration of CCN.  This discrepancy arises from the assumptions made when constructing the

465    aerosol initial and boundary conditions, which is the assumptions regarding the aerosol mode ratio

466    of SO$_4$ (80% for Aiken mode and 20% for accumulation mode).

467    The CCN calculation presented in Fig. 7a is based on the Köhler theory, which considers

468    both the aerosol size (curvature effect) and the chemical composition (solution effect) to estimate

469    the theoretical CCN number concentration at different supersaturations.    Under 1.0%

470    supersaturation, the CCN number concentration is found to be 42% of the total number of aerosol

471    number (could be estimated from 100% of accumulation mode and 16% of Aiken mode) (Fig.

472    S6a).  In the simulation of 20160701_control, the CCN number concentration under 0.2% (0.5%)

473    supersaturation is only 11% (25%) of the total aerosol number, which is lower than the

474    observations reported in Wang et al. (2020), where the observed CCN number concentration under

475    0.35% supersaturation was approximately 25% of the total aerosol number.  Even though $SO_4$ is

476    the dominant chemical component, accounting for nearly 50% (as shown in Figs. 7b and 7c), the

477    presence of an excessive number of Aiken mode aerosols may be the primary reason for the low

478    activation rate.  The curvature effect caused by these Aiken mode aerosols hinders their ability to

479    act as CCN effectively.

480    In the simulation of 20170719_control, the most aerosols within a height of 1000 m, which

481    is also the cloud layer (Fig. 7d).  The average aerosol number concentration across the entire

482    domain is measured to be 1286 $cm^{-3}$ within a height of 2000 m and the Aiken mode is 80% of the

483    total aerosol number in this case.  The chemical composition of aerosols in the 20170719_control

484    mainly is $SO_4$, and "others" (like sea salts) is second (Figs. 7e and 7f).  This variation in vertical

485    distribution leads to more aerosols being activated under the cloud top at a height of 1500 m.  This

486    is attributed to the presence of a peak value of accumulation mode aerosols and $SO_4$ at this height.

487    Because of high Aiken mode aerosols in this simulation, overall, the activation rate is low.

488    Under 1.0% supersaturation, the CCN number concentration is estimated to be 25% of the total

489    aerosol number.  This could be a result of 100% of the accumulation mode aerosols and 7% of the

490    Aiken mode aerosols contributing to the CCN population (Fig. S6c). The CCN number

491    concentration under 0.2% (0.5%) supersaturation is only 4% (12%) of the total aerosol number.

492        Among the three cases studied, the case of 20190823 stands out as the most polluted case,

493    but the aerosol component and vertical distribution are close to the case of 20170719 (Figs. 7c and

494    7i). The average aerosol number concentration across the entire domain is measured to be 1850

495    $cm^{-3}$ within a height of 2000 m. The Aiken mode aerosols are also high and contribute to more

496    than 75% of the total aerosol number in this case (Figs. 7g and S6e). High $SO_4$ component also

497    leads to more aerosols being activated under the cloud top at a height of 2000 m. The CCN number

498    concentration under 0.2% (0.5%) supersaturation is only 6% (17%) of the total aerosol number,

499    slightly better than the case of 20170719.

500        The cloud droplet numbers observed in the three cases fall within the range of CCN

501    numbers under 0.1% and 0.2% supersaturation. Therefore, in the subsequent sections, we utilize

502    the CCN number concentration under 0.2% supersaturation as a representative of the CCN

503    activation rate.

504    ## 3.3  Cloud responses to aerosol perturbations

505        Figure 8 illustrates the comparison of time series profiles of cloud water content (CWC)

506    and CCN number concentration under 0.2% supersaturation between the control runs and

507    perturbed runs. This figure also demonstrates the CCN spatiotemporal variation in our

508    simulations. Specifically, for the case of 20160701, it is evident that the CWC in

509    20160701_perturbed exhibits a positive response to increased CCN compared to the CWC in

510    20160701_control. This result aligns with the most of WRF studies that use fixed or prescribed

511    CCN numbers to investigate aerosol-cloud interactions (Wang et al., 2020; Christensen et al.,

512    2024).

513    Figure 9a depicts the time series of domain-averaged LWP, encompassing both cloud and

514    rain, and CCN number concentration under 0.2% supersaturation for both the 20160701_control

515    and 20160701_perturbed cases.  This visualization provides a quantitative representation of the

516    change in CCN number concentration, which increases from a mean value of 32.52 cm$^{-3}$ in the

517    control run to 127.68 cm$^{-3}$ in the perturbed run, approximately three times higher than the control

518    run.  Because we want to avoid counting high CCN number concentration above cloud top which

519    are also hard to become cloud droplets, the CCN number concentration is averaged within 1000 m

520    height (Wang et al., 2020).

521    The LWP in the 20160701_control case exhibits a domain mean value of 64.88 g m$^{-2}$,

522    which subsequently increases to 123.27 g m$^{-2}$ in the 20160701_perturbed case.  As mentioned in

523    Section 3.1, the LWP for the 20160701 case follows a diurnal cycle, with higher values during

524    nighttime and lower values during daytime.  This diurnal cycle is also observed in the perturbed

525    simulation, with the larger differences in CCN and LWP between the control run and perturbed

526    run during nighttime (Fig. 9a).

527    After increasing aerosols, the cloud droplet number in the 20160701_perturbed run

528    demonstrates similar responses.  In the 20160701_control case, the domain mean value of cloud

529    droplet number is 14.03 cm$^{-3}$, which subsequently increases to 45.52 cm$^{-3}$ in the

530    20160701_perturbed case.  As the cloud droplet number increases, the cloud radius decreases from

531    12.23 μm in the control run to 10.08 μm in the perturbed case.

532    The case of 20170719 represents a post-trough weather regime, and Fig. 8c illustrates the

533    passage of a frontal system in the area after 9 UTC on that day.  In the 20170719_perturbed

534    simulation, the CWC increases following the system's passage (Fig. 8d) compared to the CWC in

535    the 20170719_control run.  Additionally, the ambient CCN number in the perturbed run is also

23

536    higher.  The time variation of CCN concentration in Fig. 9c shows elevated CCN numbers before

537    and after the system enters the domain.  In the 20170719_control case, the domain mean value of

538    CCN number concentration is 60.51 cm$^{-3}$, which subsequently increases to 253.51 cm$^{-3}$ in the

539    20170719_perturbed case.  The domain-averaged LWP also exhibits an increase, rising from 59.31

540    g m$^{-2}$ in the 20170719_control run to 74.07 g m$^{-2}$ in the 20170719_perturbed case.  Notably, this

541    change primarily occurs after the passage of the frontal system.

542    The cloud droplet number consistently shows higher values in the perturbed case (Fig. 9d),

543    and this pattern is similar to the difference in CCN between the two runs of 20170719 (Fig. 9c).

544    In the 20170719_control case, the domain mean value of cloud droplet number is 20.70 cm$^{-3}$, while

545    the value is 56.09 cm$^{-3}$ in the perturbed case.  When the cloud droplet number increases in the

546    perturbed run, the cloud radius decreases from 9.90 μm in the control run to 7.49 μm in the

547    perturbed case.  This reduction in cloud radius is even smaller than the cloud radius observed in

548    the case of 20160701.

549    The case of 20190823 is similar to the case of 20170719, but it represents a weak trough

550    weather regime.  Figure 8e also illustrates the passage of a cloud system in the area between 6

551    UTC to 18 UTC on 23 August 2019, and the CWC in the perturbed run increases during this period.

552    Quantitatively, in the 20190823_control case, the domain mean value of CCN number

553    concentration is 124.32 cm$^{-3}$, which subsequently increases to 475.37 cm$^{-3}$ in the

554    20190823_perturbed case, which is also about three times higher.  The domain-averaged LWP

555    also exhibits an increase, rising from 48.92 g m$^{-2}$ in the 20190823_control run to 58.53 g m$^{-2}$ in

556    the 20190823_perturbed case.

557    Differ from the case of 20170719, the frontal system moved away from the study domain

558    after 12 UTC, the differences of CCN number or cloud droplet number between the control and

559     perturbed runs becomes even more pronounced after the system (Figs. 9e and 9f). In the

560     20190823_control case, the domain mean value of cloud droplet number is 33.94 cm$^{-3}$, while the

561     value is 79.97 cm$^{-3}$ in the perturbed case. When the cloud droplet number increases in the

562     perturbed run, the cloud radius decreases from 8.51 μm in the control run to 6.45 μm in the

563     perturbed case. This reduction in cloud radius is similar to the cloud radius observed in the case

564     of 20170719.

565     We observe that large aerosol-induced LWP occurs during the periods of rainfall (Fig. S7).

566     To accurately quantify the differences, we calculate the average LWP over approximately 25 km

567     of the domain 4. This results in 16 averaged grids per output file, with each file generated every

568     10 minutes. This averaging process is based on Arola et al. (2022) and Zhou and Feingold (2023)

569     to avoid the impact of heterogeneity and co-variability on the results. Specifically, we aggregate

570     the simulation grids with a spacing resolution of approximately 190 m to form a larger grid of

571     around 25 km for each 10-minute simulation output, as presented in Table 2.

572     Table 2 presents the 10-minute mean and standard deviation of several variables, including

573     CCN, LWP, cloud droplet number (Nc), cloud radius (Re), and rainfall intensity (RI), across three

574     study cases. The classification of "rain" and "non-rain" is based on the RI (unit: mm hr$^{-1}$) on the

575     averaged grid. Specifically, a grid is considered as "rain" if the RI is greater than zero. In the

576     control cases, the averaged CCN number is 73.07 cm$^{-3}$, and the corresponding LWP is 53.17 g m$^{-}$

577     $^{2}$. However, in the perturbed cases, the CCN number increases approximately threefold, reaching

578     218.21 cm$^{-3}$, and the LWP increases by 49% to 79.25 g m$^{-2}$. The introduction of additional aerosols

579     in the perturbed cases also leads to a significant increase in the Nc number, from 22.68 cm$^{-3}$ in the

580     control cases to 59.74 cm$^{-3}$ in the perturbed cases. Consequently, the Re decreases by 21% from

581     9.97 μm to 7.83 μm, and the RI decreases by 11% from 0.009 mm hr$^{-1}$ to 0.008 mm hr$^{-1}$.

582       To investigate the interaction between aerosols and clouds, we analyze the results

583    separately for rain and non-rain grids. In both the control and perturbed cases, we observe that the

584    CCN number within 1000 m is lower in the rain grids compared to the non-rain grids, primarily

585    due to the washout effect caused by rainfall. Additionally, the LWP over the rain grids is generally

586    higher than that over the non-rain grids. Furthermore, when comparing the control and perturbed

587    cases, we find that the LWP over the rain grids increases by 57% from 58.57 g m$^{-2}$ to 91.81 g m$^{-2}$.

588    In contrast, the LWP over the non-rain grids only increases by 28% (Table 2). This difference can

589    be attributed to the conversion of cloud droplets to raindrops through processes like autoconversion

590    and collection, which occurs more prominently over the rain grids. We also observe that in the

591    non-rain grids, especially at the cloud edges (or low LWP), the perturbed cases reveal an increased

592    presence of small cloud droplets. This abundance of smaller droplets facilitates evaporation,

593    resulting in a reduced LWP (e.g., clouds in the bottom right corner of Figs. S8a and S8b).

594    Consequently, the Nc number over the rain grids is lower compared to the Nc number over the

595    non-rain grids. Moreover, when introducing aerosols in the perturbed runs, the results over the

596    rain grids exhibit larger cloud drops and a wider radius spectrum compared to the results over the

597    non-rain grids. This suggests that the presence of aerosols has a more pronounced effect on cloud

598    properties within the rain grids.

599       Zheng et al. (2022) conducted a study on the aerosol-cloud interaction using ground-based

600    measurements from the ARM program, focusing on the influence of environmental variables.

601    Their findings revealed that when there is ample water vapor and low CCN loading, the active

602    coalescence process leads to a broader size distribution of cloud droplets, resulting in an increase

603    in cloud droplet radius. On the other hand, when there is enhanced activation of CCN and

604    condensational growth of cloud droplets due to higher CCN loading below the cloud, the cloud

605   droplet radius decreases. This combined effect signifies an intensified aerosol-cloud interaction,

606   leading to a broad range of cloud droplet radii. The simulated results in our study, specifically

607   over the rain grids where a sufficient water vapor environment is considered, demonstrate a

608   significant aerosol-cloud interaction, where increased CCN introduces more newly converted

609   droplets, resulting in a broad range of cloud droplet radii.

610      Since we utilize a comprehensive aerosol module in WRF-Chem to examine aerosol-cloud

611   interactions, we are able to explore how changes in cloud properties, driven by increased CCN,

612   affect aerosol concentrations. For example, in the post-trough regime (20170917 case) and the

613   weak trough regime (20190823 case), we observe that the cloud structure exhibits more open-cell

614   stratocumulus clouds (Figs. 2h and 2i). As motioned above, the increased number of smaller cloud

615   droplets at the cloud edge facilitate evaporation and results in a lower LWP (Fig. S8). The larger

616   aerosols from the evaporated clouds return to the accumulation mode, making them more likely to

617   activate as CCN again.

618      To demonstrate how robust this process on the ACI, we calculate the time series of the

619   ratio of the percentage of activated CCN at 0.2% supersaturation to the accumulation mode

620   aerosols       between       perturbed       and       control       runs,       defined

621   as $\left. (CCN_{0.2\%}/Accu.\,aerosols)_{perturbed} \middle/ (CCN_{0.2\%}/Accu.\,aerosols)_{control} \right.$, shown in Fig. 10. A

622   ratio greater than 1 suggests that accumulation mode aerosols in the perturbed cases are more

623   readily activated as CCN at a supersaturation of 0.2%, especially in the cases of 20170719 and

624   20190823. Conversely, a ratio less than 1 is observed during the first half of the day in the

625   20170701 case, which is attributed to the very low levels of accumulation mode aerosols in the

626   model.

27

### 3.4 Cloud liquid water path (LWP) susceptibilities

627

628       In this study, the susceptibility of LWP to changes in CCN concentration is quantified

629 using the logarithmic slope between LWP and CCN, denoted as $dln(LWP)/dln(CCN)$

630 (Gryspeerdt et al., 2019). This slope represents the sensitivity of warm stratocumulus clouds' LWP

631 to variations in CCN concentration, like shown in Fig. S8c. As presented in Table 2, we aggregate

632 the simulation grids with a spacing resolution of approximately 190 m to form a larger grid of

633 around 25 km for each 10-minute simulation output. This averaging process helps to reduce the

634 impact of heterogeneity and co-variability on the results.

635       Figure 11 illustrates the averaged cloud susceptibilities for various LWP and CCN or Nc

636 bins across three study periods. The logarithmic slope between LWP and CCN is calculated at

637 each output time (every 10 minutes) using data from 16 aggregated grid points from the control

638 run and 16 aggregated grid points from the perturbed run. Our study reveals that when the CCN

639 concentration is below 100 cm$^{-3}$, the susceptibility for different LWP and CCN values is positive

640 and the values are large, indicating that changes in LWP are sensitive to variations in CCN number.

641 Here also demonstrates the AIE is large when an increase in CCN can have a large impact on LWP

642 enhancement. However, when the mean CCN concentration exceeds 100 cm$^{-3}$, the LWP

643 susceptibility becomes small, both positive and negative. This suggests that the change in LWP is

644 not as sensitive to changes in CCN number (as shown in Fig. 11a). It is important to note that the

645 CCN number used in our study is averaged within a 1000 m range, which may introduce

646 uncertainty to the absolute values of susceptibility by including aerosols that are not directly

647 involved in the aerosol-cloud interaction (Wang et al., 2020).

648       Additionally, our simulations indicate that the Nc in this study is generally low, with a

649 mean value typically below 80 cm$^{-3}$. For different LWP and Nc values, the susceptibility is mostly

650    positive, indicating that changes in LWP are sensitive to variations in Nc number (as shown in Fig.

651    11c).

652         When we investigate the variation of LWP susceptibility over time, we observe that

653    positive susceptibilities for different LWP and CCN (Nc) typically occur during periods of no rain

654    or light rain (Figs. 12 and S7).  On 1 July 2016, the time series of LWP susceptibility for different

655    CCN or Nc shows a diurnal cycle, with large positive values during the nighttime and small

656    positive values in the afternoon.  During heavy rain events, such as from 9 to 16 UTC on 19 July

657    2017 and from 0 to 15 UTC on 23 August 2019 (Fig. S7), the LWP susceptibilities are negative or

658    close to zero (Figs. 12c and 12e).  In the perturbed cases, during the heavy rainfall periods, some

659    aggregated grids show very low LWP (Fig. S8c).  This reduction in LWP is caused by the

660    evaporation from small cloud droplets at non-rain grids on the cloud edge.  Those low LWP grids

661    in the perturbed runs result in a negative or near-zero logarithmic slope between LWP and CCN

662    (Figs. S8c, 12c and 12e), although the domain mean LWP is higher in the perturbed case than in

663    the control case (Figs. 9c and 9e).

664         To further illustrate the reduction in LWP due to evaporation at the cloud edge, Fig. 13

665    presents the relative change in $ln(LWP)$  between the perturbed and control cases across different

666    LWP percentile ranges in the control case during the periods of negative LWP susceptibility, as

667    shown in Fig. 12.  The results indicate a decrease in LWP in the perturbed cases compared to the

668    control cases for pixels with the lowest LWP percentile range (0-25%), which we assume occur at

669    the cloud edges.

670         Figures 11b and 11d display the mean Re susceptibilities for different CCN and Nc,

671    respectively.  The results consistently show that as CCN or Nc increases, the radius of the cloud

672  droplets decreases. Additionally, the change in Re is more pronounced when the Nc (or CCN) is

673  higher.

# 4  Discussion and summary

675  This study focuses on aerosol indirect effects (AIE), particularly involving long-range

676  transport aerosols, in the Eastern North Atlantic (ENA) region. It specifically examines these

677  effects on warm boundary layer stratiform clouds located on the eastern side of oceanic subtropical

678  highs under three different weather regimes: a ridge with a surface high-pressure system, a post-

679  trough with a surface high-pressure system, and a weak trough. We select three specific study

680  cases (i.e., 20160701, 20170719, and 20190823) to assess the impact of long-range transport

681  aerosols on warm boundary layer clouds, with each case representing a typical meteorological

682  regime observed over the ENA site.

683  To investigate aerosol-cloud interactions more realistically, incorporating aerosol

684  chemistry components that activate to cloud condensation nuclei (CCN) and accounting for aerosol

685  spatiotemporal variation, this study employs the Weather Research and Forecast model coupled

686  with a chemistry component (WRF-Chem). This approach provides a detailed examination of AIE

687  in the ENA region under the three specified weather regimes. We employ a downscaling technique

688  to conduct WRF-Chem simulations for the two inner domains (with the outer domains utilizing

689  WRF). This approach results in nearly a 50% reduction in total computational costs, achieving a

690  throughput of 8 hours per day using 1,080 cores.

691  We incorporate major aerosol species (BC, OC, and $SO_4$), as well as $SO_2$, from MERRA-

692  2 to provide aerosol initial and boundary conditions, labeled as control cases. Additionally, we

693  formulate three perturbed cases by amplifying aerosol concentrations in both initial and boundary

694  conditions, as well as sea salt emissions, by a factor of five relative to each control case. Since

695   aerosol features are primarily determined by aerosol initial and boundary conditions, a higher

696   Aiken mode assumption in the major aerosol component (i.e., $SO_4$) regarding the aerosol mode

697   ratio (80% for Aiken mode and 20% for accumulation mode) results in fewer aerosols activating

698   as CCN due to the curvature effect in our simulations.

699        The WRF-Chem model captures the cloud structure in the case of 20160701. It simulates

700   the formation of thin, uniform stratocumulus clouds within a meteorological regime characterized

701   by a ridge system in the free troposphere and a high-pressure system near the surface. However,

702   the cases of 20170719 and 20190823 exhibit the development of broke and thicker solid

703   stratocumulus clouds within a post-trough regime and a weak trough, respectively. With the fast-

704   moving cloud systems and strong surface wind, the WRF-Chem model struggle to capture the

705   development and movement of these cloud systems due to delayed moisture transport from outer

706   boundary condition and potential insufficient vertical resolution.

707        In all cases, compared to the observations, the WRF-Chem model underestimates the liquid

708   water path (LWP) and cloud fraction due to warmer and lower simulated boundary layer. In the

709   perturbed cases, we find 57% higher aerosol-induced LWP, especially during the periods of

710   rainfall. We also note that the perturbed cases exhibit lower rainfall intensity, indicating a rainfall

711   suppression effect attributed to high CCN concentrations as concluded in previous studies (Wang

712   et al., 2020; Christensen et al., 2024). In contrast, the LWP over the non-rain grids only increases

713   by 28%. Moreover, when introducing aerosols in the perturbed runs, the results over the rain grids

714   exhibit larger cloud drops and a wider radius spectrum compared to the results over the non-rain

715   grids. This suggests that the presence of aerosols has a more pronounced effect on cloud properties

716   within the rain grids. The non-rain grids over the cloud edge can have lower LWP because smaller

717   cloud droplets are easy to evaporate.

718    Our study further elucidates the intricate feedback mechanisms governing aerosol-cloud

719    interactions and aerosol properties. In both the post-trough and weak trough regimes, we observe

720    a pronounced tendency for the cloud structure to develop more open-cell stratocumulus clouds.

721    At the peripheries of these clouds, the perturbed cases demonstrate a significant increase in the

722    presence of small cloud droplets. This heightened abundance of smaller droplets not only

723    promotes evaporation but also leads to a marked reduction in LWP.

724    As these clouds evaporate, the larger aerosols that are released return to the accumulation

725    mode. This transition enhances their likelihood of reactivating as CCN. Consequently, this cycle

726    underscores the dynamic interplay between aerosol properties and cloud formation, highlighting

727    how changes in aerosol concentrations can influence cloud microphysics and, ultimately,

728    precipitation processes.

729    Additionally, the susceptibility of LWP to changes in CCN concentration is quantified

730    using the logarithmic slope between LWP and CCN. Our result shows when the CCN

731    concentration is low, LWP is sensitive to variations in CCN number, with higher CCN number

732    concentration leading to higher LWP. However, when the mean CCN concentration is relatively

733    high, LWP is not as sensitive to changes in CCN, the LWP susceptibilities are small in magnitude,

734    with both positive and negative values. Those negative values are caused by the evaporation from

735    small cloud droplets at non-rain grids on the cloud edge.

736    In Wang et al. (2020), the LWC susceptibility for a light precipitation case on 18 July 2017

737    also shows positive values based on three sensitivity runs with CCN concentrations of 10, 100,

738    and 1000 cm$^{-3}$. The cloud properties in their study are averaged over all cloud points in the

739    innermost domain. We adopt the same method as Wang et al. (2020) to estimate the LWP

740    susceptibility          using          the          domain          mean          values,          defined          as

741 $\Delta ln\left(LWP_{perturbed} - LWP_{control}\right)/\Delta ln\left(CCN_{perturbed} - CCN_{control}\right)$. This approach

742 predominantly yields positive values for LWP susceptibility across the three study cases (see Figs.

743 S9 and S10). This suggests that the 25-km resolution is critical for accurately estimating LWP

744 susceptibility. A resolution that is too coarse (i.e., using the domain mean) may fail to capture

745 finer details, such as the aerosol drying effects occurring at the cloud edges.

746 Conversely, the LWP susceptibilities associated with varying cloud droplet numbers

747 reported in Qiu et al. (2024) reveal significant negative values in LWP susceptibility in response

748 to high cloud droplet numbers, a trend that is partially reflected in our study. Further investigation

749 is required to reconcile the difference in LWP responses between observational data and model

750 simulations. Additionally, a more accurate estimation of LWP susceptibility to changes in CCN

751 concentration is necessary.

752

753 **Code and data availability:**

754 The WRF-Chem code (v4.4.2) used in this study has been released on GitHub

755 (https://github.com/wrf-model/WRF/releases/download/v4.4.2/v4.4.2.tar.gz). The observational

756 data used in this study are available at https://doi.org/10.5281/zenodo.13356995. Other WRF-

757 Chem simulated outputs for the plots in this paper are available at

758 https://doi.org/10.5281/zenodo.13357040.

759

760 **Author contributions:**

761     H.-H. Lee and X. Zheng provided ideas and designed the experiments in this study.  H.-H. Lee

762     conducted all the simulations and analyses.  H.-H. Lee leads and coordinates the manuscript with

763     inputs from coauthors.

764

**Competing interests.**

766     At least one of the (co-)authors is a member of the editorial board of Atmospheric Chemistry and

767     Physics.

768

774

**Reference:**

776     Abdul-Razzak, H. and Ghan, S. J.: A parameterization of aerosol activation: 2. Multiple
777     aerosol types, Journal of Geophysical Research: Atmospheres, 105, 6837-6844,
778     https://doi.org/10.1029/1999JD901161, 2000.
779     Ackermann, I. J., Hass, H., Memmesheimer, M., Ebel, A., Binkowski, F. S., and Shankar, U.:
780     Modal aerosol dynamics model for Europe: development and first applications,
781     Atmospheric Environment, 32, 2981-2999, http://dx.doi.org/10.1016/S1352-
782     2310(98)00006-5, 1998.
783     Albrecht, B. A.: Aerosols, Cloud Microphysics, and Fractional Cloudiness, Science, 245,
784     1227-1230, doi:10.1126/science.245.4923.1227, 1989.

785    Arola, A., Lipponen, A., Kolmonen, P., Virtanen, T. H., Bellouin, N., Grosvenor, D. P.,
786    Gryspeerdt, E., Quaas, J., and Kokkola, H.: Aerosol effects on clouds are concealed by
787    natural cloud heterogeneity and satellite retrieval errors, Nature Communications, 13,
788    7357, 10.1038/s41467-022-34948-5, 2022.
789    Binkowski, F. S. and Shankar, U.: The Regional Particulate Matter Model: 1. Model
790    description and preliminary results, Journal of Geophysical Research: Atmospheres, 100,
791    26191-26209, https://doi.org/10.1029/95JD02093, 1995.
792    Cadeddu, M. P., Ghate, V. P., and Mech, M.: Ground-based observations of cloud and
793    drizzle liquid water path in stratocumulus clouds, Atmos. Meas. Tech., 13, 1485-1499,
794    10.5194/amt-13-1485-2020, 2020.
795    Chapman, E. G., Gustafson Jr, W. I., Easter, R. C., Barnard, J. C., Ghan, S. J., Pekour, M. S.,
796    and Fast, J. D.: Coupling aerosol-cloud-radiative processes in the WRF-Chem model:
797    Investigating the radiative impact of elevated point sources, Atmos. Chem. Phys., 9, 945-
798    964, 10.5194/acp-9-945-2009, 2009.
799    Chen, F. and Dudhia, J.: Coupling an Advanced Land Surface–Hydrology Model with the
800    Penn State–NCAR MM5 Modeling System. Part I: Model Implementation and Sensitivity,
801    Monthly Weather Review, 129, 569-585, https://doi.org/10.1175/1520-
802    0493(2001)129<0569:CAALSH>2.0.CO;2, 2001.
803    Chen, T., Rossow, W. B., and Zhang, Y.: Radiative Effects of Cloud-Type Variations, Journal
804    of Climate, 13, 264-286, 10.1175/1520-0442(2000)013<0264:Reoctv>2.0.Co;2, 2000.
805    Chin, M., Ginoux, P., Kinne, S., Torres, O., Holben, B. N., Duncan, B. N., Martin, R. V.,
806    Logan, J. A., Higurashi, A., and Nakajima, T.: Tropospheric Aerosol Optical Thickness from
807    the GOCART Model and Comparisons with Satellite and Sun Photometer Measurements,
808    Journal of the Atmospheric Sciences, 59, 461-483, https://doi.org/10.1175/1520-
809    0469(2002)059<0461:TAOTFT>2.0.CO;2, 2002.
810    Christensen, M. W., Wu, P., Varble, A. C., Xiao, H., and Fast, J. D.: Aerosol-induced closure
811    of marine cloud cells: enhanced effects in the presence of precipitation, Atmos. Chem.
812    Phys., 24, 6455-6476, 10.5194/acp-24-6455-2024, 2024.
813    Clarke, A. D., Owens, S. R., and Zhou, J.: An ultrafine sea-salt flux from breaking waves:
814    Implications for cloud condensation nuclei in the remote marine atmosphere, Journal of
815    Geophysical Research: Atmospheres, 111, https://doi.org/10.1029/2005JD006565, 2006.
816    Fast, J. D., Gustafson Jr., W. I., Easter, R. C., Zaveri, R. A., Barnard, J. C., Chapman, E. G.,
817    Grell, G. A., and Peckham, S. E.: Evolution of ozone, particulates, and aerosol direct
818    radiative forcing in the vicinity of Houston using a fully coupled meteorology-chemistry-
819    aerosol model, Journal of Geophysical Research: Atmospheres, 111,
820    https://doi.org/10.1029/2005JD006721, 2006.
821    Feingold, G., Ghate, V. P., Russell, L. M., Blossey, P., Cantrell, W., Christensen, M. W.,
822    Diamond, M. S., Gettelman, A., Glassmeier, F., Gryspeerdt, E., Haywood, J., Hoffmann, F.,
823    Kaul, C. M., Lebsock, M., McComiskey, A. C., McCoy, D. T., Ming, Y., Mülmenstädt, J.,
824    Possner, A., Prabhakaran, P., Quinn, P. K., Schmidt, K. S., Shaw, R. A., Singer, C. E.,
825    Sorooshian, A., Toll, V., Wan, J. S., Wood, R., Yang, F., Zhang, J., and Zheng, X.: Physical
826    science research needed to evaluate the viability and risks of marine cloud brightening,
827    Science Advances, 10, eadi8594, doi:10.1126/sciadv.adi8594, 2024.

828    Gallo, F., Uin, J., Sanchez, K. J., Moore, R. H., Wang, J., Wood, R., Mei, F., Flynn, C.,
829    Springston, S., Azevedo, E. B., Kuang, C., and Aiken, A. C.: Long-range transported
830    continental aerosol in the eastern North Atlantic: three multiday event regimes influence
831    cloud condensation nuclei, Atmos. Chem. Phys., 23, 4221-4246, 10.5194/acp-23-4221-
832    2023, 2023.
833    Ghate, V. P. and Cadeddu, M. P.: Drizzle and Turbulence Below Closed Cellular Marine
834    Stratocumulus Clouds, Journal of Geophysical Research: Atmospheres, 124, 5724-5737,
835    https://doi.org/10.1029/2018JD030141, 2019.
836    Ghate, V. P., Surleta, T., Magaritz-Ronen, L., Raveh-Rubin, S., Gallo, F., Carlton, A. G., and
837    Azevedo, E. B.: Drivers of Cloud Condensation Nuclei in the Eastern North Atlantic as
838    Observed at the ARM Site, Journal of Geophysical Research: Atmospheres, 128,
839    e2023JD038636, https://doi.org/10.1029/2023JD038636, 2023.
840    Gong, S. L.: A parameterization of sea-salt aerosol source function for sub- and super-
841    micron particles, Global Biogeochemical Cycles, 17,
842    https://doi.org/10.1029/2003GB002079, 2003.
843    Grell, G. A., Peckham, S. E., Schmitz, R., McKeen, S. A., Frost, G., Skamarock, W. C., and
844    Eder, B.: Fully coupled "online" chemistry within the WRF model, Atmospheric
845    Environment, 39, 6957-6975, https://doi.org/10.1016/j.atmosenv.2005.04.027, 2005.
846    Gryspeerdt, E., Goren, T., Sourdeval, O., Quaas, J., Mülmenstädt, J., Dipu, S., Unglaub, C.,
847    Gettelman, A., and Christensen, M.: Constraining the aerosol influence on cloud liquid
848    water path, Atmos. Chem. Phys., 19, 5331-5347, 10.5194/acp-19-5331-2019, 2019.
849    Hartmann, D. L., Ockert-Bell, M. E., and Michelsen, M. L.: The Effect of Cloud Type on
850    Earth's Energy Balance: Global Analysis, Journal of Climate, 5, 1281-1304, 10.1175/1520-
851    0442(1992)005<1281:Teocto>2.0.Co;2, 1992.
852    Hersbach, H., Bell, B., Berrisford, P., Biavati, G., Horányi, A., Muñoz Sabater, J., Nicolas, J.,
853    Peubey, C., Radu, R., Rozum, I., Schepers, D., Simmons, A., Soci, C., Dee, D., and Thépaut,
854    J.-N.: ERA5 hourly data on single levels from 1940 to present. Copernicus Climate Change
855    Service (C3S) Climate Data Store (CDS) [dataset], 10.24381/cds.adbb2d47 2023.
856    Hong, S.-Y. and Jang, J.: Impacts of Shallow Convection Processes on a Simulated Boreal
857    Summer Climatology in a Global Atmospheric Model, Asia-Pacific Journal of Atmospheric
858    Sciences, 54, 361-370, 10.1007/s13143-018-0013-3, 2018.
859    Iacono, M. J., Delamere, J. S., Mlawer, E. J., Shephard, M. W., Clough, S. A., and Collins, W.
860    D.: Radiative forcing by long-lived greenhouse gases: Calculations with the AER radiative
861    transfer models, Journal of Geophysical Research: Atmospheres, 113,
862    10.1029/2008jd009944, 2008.
863    Janjić, Z. I.: The Step-Mountain Eta Coordinate Model: Further Developments of the
864    Convection, Viscous Sublayer, and Turbulence Closure Schemes, Monthly Weather
865    Review, 122, 927-945, https://doi.org/10.1175/1520-
866    0493(1994)122<0927:TSMECM>2.0.CO;2, 1994.
867    kazemirad, M. and Miller, M. A.: Summertime Post-Cold-Frontal Marine Stratocumulus
868    Transition Processes over the Eastern North Atlantic, Journal of the Atmospheric Sciences,
869    77, 2011-2037, https://doi.org/10.1175/JAS-D-19-0167.1, 2020.

870  Kazil, J., Wang, H., Feingold, G., Clarke, A. D., Snider, J. R., and Bandy, A. R.: Modeling
871  chemical and aerosol processes in the transition from closed to open cells during
872  VOCALS-REx, Atmos. Chem. Phys., 11, 7491-7514, 10.5194/acp-11-7491-2011, 2011.
873  Klein, S. A. and Hartmann, D. L.: The Seasonal Cycle of Low Stratiform Clouds, Journal of
874  Climate, 6, 1587-1606, 10.1175/1520-0442(1993)006<1587:Tscols>2.0.Co;2, 1993.
875  Knievel, J. C., Bryan, G. H., and Hacker, J. P.: Explicit Numerical Diffusion in the WRF
876  Model, Monthly Weather Review, 135, 3808-3824,
877  https://doi.org/10.1175/2007MWR2100.1, 2007.
878  Lee, S. S., Donner, L. J., Phillips, V. T. J., and Ming, Y.: The dependence of aerosol effects on
879  clouds and precipitation on cloud-system organization, shear and stability, Journal of
880  Geophysical Research: Atmospheres, 113, https://doi.org/10.1029/2007JD009224, 2008.
881  Liljegren, J. C., Clothiaux, E. E., Mace, G. G., Kato, S., and Dong, X.: A new retrieval for
882  cloud liquid water path using a ground-based microwave radiometer and measurements of
883  cloud temperature, Journal of Geophysical Research: Atmospheres, 106, 14485-14500,
884  https://doi.org/10.1029/2000JD900817, 2001.
885  Liu, X., Easter, R. C., Ghan, S. J., Zaveri, R., Rasch, P., Shi, X., Lamarque, J. F., Gettelman,
886  A., Morrison, H., Vitt, F., Conley, A., Park, S., Neale, R., Hannay, C., Ekman, A. M. L., Hess,
887  P., Mahowald, N., Collins, W., Iacono, M. J., Bretherton, C. S., Flanner, M. G., and Mitchell,
888  D.: Toward a minimal representation of aerosols in climate models: description and
889  evaluation in the Community Atmosphere Model CAM5, Geosci. Model Dev., 5, 709-739,
890  10.5194/gmd-5-709-2012, 2012.
891  Logan, T., Xi, B., and Dong, X.: Aerosol properties and their influences on marine boundary
892  layer cloud condensation nuclei at the ARM mobile facility over the Azores, Journal of
893  Geophysical Research: Atmospheres, 119, 4859-4872,
894  https://doi.org/10.1002/2013JD021288, 2014.
895  Mather, J. H. and Voyles, J. W.: The Arm Climate Research Facility: A Review of Structure
896  and Capabilities, Bulletin of the American Meteorological Society, 94, 377-392,
897  https://doi.org/10.1175/BAMS-D-11-00218.1, 2013.
898  McCoy, I. L., Wyant, M. C., Blossey, P. N., Bretherton, C. S., and Wood, R.: Aitken Mode
899  Aerosols Buffer Decoupled Mid-Latitude Boundary Layer Clouds Against Precipitation
900  Depletion, Journal of Geophysical Research: Atmospheres, 129, e2023JD039572,
901  https://doi.org/10.1029/2023JD039572, 2024.
902  Mechem, D. B., Wittman, C. S., Miller, M. A., Yuter, S. E., and de Szoeke, S. P.: Joint
903  Synoptic and Cloud Variability over the Northeast Atlantic near the Azores, Journal of
904  Applied Meteorology and Climatology, 57, 1273-1290, https://doi.org/10.1175/JAMC-D-17-
905  0211.1, 2018.
906  Mellor, G. L. and Yamada, T.: Development of a turbulence closure model for geophysical
907  fluid problems, Reviews of Geophysics, 20, 851-875,
908  https://doi.org/10.1029/RG020i004p00851, 1982.
909  Minnis, P., Sun-Mack, S., Young, D. F., Heck, P. W., Garber, D. P., Chen, Y., Spangenberg,
910  D. A., Arduini, R. F., Trepte, Q. Z., Smith, W. L., Ayers, J. K., Gibson, S. C., Miller, W. F.,
911  Hong, G., Chakrapani, V., Takano, Y., Liou, K. N., Xie, Y., and Yang, P.: CERES Edition-2
912  Cloud Property Retrievals Using TRMM VIRS and Terra and Aqua MODIS Data—Part I:

913    Algorithms, IEEE Transactions on Geoscience and Remote Sensing, 49, 4374-4400,
914    10.1109/TGRS.2011.2144601, 2011.
915    Minnis, P., Sun-Mack, S., Chen, Y., Chang, F. L., Yost, C. R., Smith, W. L., Heck, P. W.,
916    Arduini, R. F., Bedka, S. T., Yi, Y., Hong, G., Jin, Z., Painemal, D., Palikonda, R., Scarino, B.
917    R., Spangenberg, D. A., Smith, R. A., Trepte, Q. Z., Yang, P., and Xie, Y.: CERES MODIS
918    Cloud Product Retrievals for Edition 4—Part I: Algorithm Changes, IEEE Transactions on
919    Geoscience and Remote Sensing, 59, 2744-2780, 10.1109/TGRS.2020.3008866, 2021.
920    Mlawer, E. J., Taubman, S. J., Brown, P. D., Iacono, M. J., and Clough, S. A.: Radiative
921    transfer for inhomogeneous atmospheres: RRTM, a validated correlated-k model for the
922    longwave, Journal of Geophysical Research: Atmospheres, 102, 16663-16682,
923    https://doi.org/10.1029/97JD00237, 1997.
924    Modeling, G. and Office, A.: MERRA-2 inst3_3d_aer_Nv: 3d, 3-hourly, instantaneous,
925    model-level, assimilation, aerosol mixing ratio V5. 12.4, 2015.
926    Molod, A., Takacs, L., Suarez, M., and Bacmeister, J.: Development of the GEOS-5
927    atmospheric general circulation model: evolution from MERRA to MERRA2, Geosci. Model
928    Dev., 8, 1339-1356, 10.5194/gmd-8-1339-2015, 2015.
929    Monin, A. S. and Obukhov, A. M.: Basic laws of turulent mixing in the atmosphere near the
930    ground, Tr. Inst. Teor. Geofiz. Akad. Nauk SSSR, 24, 1963-1987, 1954.
931    Morrison, H., Thompson, G., and Tatarskii, V.: Impact of Cloud Microphysics on the
932    Development of Trailing Stratiform Precipitation in a Simulated Squall Line: Comparison of
933    One- and Two-Moment Schemes, Monthly Weather Review, 137, 991-1007,
934    https://doi.org/10.1175/2008MWR2556.1, 2009.
935    Painemal, D., Spangenberg, D., Smith Jr, W. L., Minnis, P., Cairns, B., Moore, R. H.,
936    Crosbie, E., Robinson, C., Thornhill, K. L., Winstead, E. L., and Ziemba, L.: Evaluation of
937    satellite retrievals of liquid clouds from the GOES-13 imager and MODIS over the
938    midlatitude North Atlantic during the NAAMES campaign, Atmos. Meas. Tech., 14, 6633-
939    6646, 10.5194/amt-14-6633-2021, 2021.
940    Qiu, S., Zheng, X., Painemal, D., Terai, C. R., and Zhou, X.: Daytime variation in the aerosol
941    indirect effect for warm marine boundary layer clouds in the eastern North Atlantic, Atmos.
942    Chem. Phys., 24, 2913-2935, 10.5194/acp-24-2913-2024, 2024.
943    Rémillard, J. and Tselioudis, G.: Cloud Regime Variability over the Azores and Its
944    Application to Climate Model Evaluation, Journal of Climate, 28, 9707-9720,
945    https://doi.org/10.1175/JCLI-D-15-0066.1, 2015.
946    Schell, B., Ackermann, I. J., Hass, H., Binkowski, F. S., and Ebel, A.: Modeling the formation
947    of secondary organic aerosol within a comprehensive air quality model system, Journal of
948    Geophysical Research: Atmospheres (1984–2012), 106, 28275-28293, 2001.
949    Skamarock, W., Klemp, J., Dudhia, J., Gill, D., Liu, Z., Berner, J., and Huang, X.: A
950    description of the advanced research WRF model version 4.3 (No. NCAR/TN-556+
951    STR).[Software], 2021.
952    Skamarock, W. C., Klemp, J. B., Dudhia, J., Gill, D. O., Barker, D. M., Duda, M. G., Huang,
953    X.-Y., Wang, W., and Powers, J. G.: A description of the advanced research WRF version 3,
954    NCAR technical note, 475, 10.5065, 2008.

955 Stephens, G. L. and Greenwald, T. J.: The Earth's radiation budget and its relation to
956 atmospheric hydrology: 2. Observations of cloud effects, Journal of Geophysical Research:
957 Atmospheres, 96, 15325-15340, 10.1029/91jd00972, 1991.
958 Stockwell, W. R., Kirchner, F., Kuhn, M., and Seefeld, S.: A new mechanism for regional
959 atmospheric chemistry modeling, Journal of Geophysical Research: Atmospheres, 102,
960 25847-25879, 10.1029/97JD00849, 1997.
961 Tian, J., Dong, X., Xi, B., Williams, C. R., and Wu, P.: Estimation of liquid water path below
962 the melting layer in stratiform precipitation systems using radar measurements during
963 MC3E, Atmos. Meas. Tech., 12, 3743-3759, 10.5194/amt-12-3743-2019, 2019.
964 Toon, O. B., Kasting, J. F., Turco, R. P., and Liu, M. S.: The sulfur cycle in the marine
965 atmosphere, Journal of Geophysical Research: Atmospheres, 92, 943-963,
966 https://doi.org/10.1029/JD092iD01p00943, 1987.
967 Tuccella, P., Curci, G., Visconti, G., Bessagnet, B., Menut, L., and Park, R. J.: Modeling of
968 gas and aerosol with WRF/Chem over Europe: Evaluation and sensitivity study, Journal of
969 Geophysical Research: Atmospheres, 117, https://doi.org/10.1029/2011JD016302, 2012.
970 Twomey, S.: Pollution and the planetary albedo, Atmospheric Environment (1967), 8, 1251-
971 1256, https://doi.org/10.1016/0004-6981(74)90004-3, 1974.
972 Twomey, S.: Aerosols, clouds and radiation, Atmospheric Environment. Part A. General
973 Topics, 25, 2435-2442, https://doi.org/10.1016/0960-1686(91)90159-5, 1991.
974 Wang, J., Wood, R., Jensen, M. P., Chiu, J. C., Liu, Y., Lamer, K., Desai, N., Giangrande, S.
975 E., Knopf, D. A., Kollias, P., Laskin, A., Liu, X., Lu, C., Mechem, D., Mei, F., Starzec, M.,
976 Tomlinson, J., Wang, Y., Yum, S. S., Zheng, G., Aiken, A. C., Azevedo, E. B., Blanchard, Y.,
977 China, S., Dong, X., Gallo, F., Gao, S., Ghate, V. P., Glienke, S., Goldberger, L., Hardin, J. C.,
978 Kuang, C., Luke, E. P., Matthews, A. A., Miller, M. A., Moffet, R., Pekour, M., Schmid, B.,
979 Sedlacek, A. J., Shaw, R. A., Shilling, J. E., Sullivan, A., Suski, K., Veghte, D. P., Weber, R.,
980 Wyant, M., Yeom, J., Zawadowicz, M., and Zhang, Z.: Aerosol and Cloud Experiments in the
981 Eastern North Atlantic (ACE-ENA), Bulletin of the American Meteorological Society, 103,
982 E619-E641, https://doi.org/10.1175/BAMS-D-19-0220.1, 2022.
983 Wang, Y., Zheng, X., Dong, X., Xi, B., Wu, P., Logan, T., and Yung, Y. L.: Impacts of long-
984 range transport of aerosols on marine-boundary-layer clouds in the eastern North Atlantic,
985 Atmos. Chem. Phys., 20, 14741-14755, 10.5194/acp-20-14741-2020, 2020.
986 Warren, S. G., Hahn, C. J., London, J., Chervin, R. M., Jenne, R. L., Colorado Univ., B., CO .
987 Cooperative Inst. for Research in Environmental Sciences, Colorado Univ., B., CO . Dept.
988 of Astrophysical, Planetary,, Sciences, A., and National Center for Atmospheric Research,
989 B., CO ): Global distribution of total cloud cover and cloud type amounts over the ocean,
990 United States, Medium: ED; Size: Pages: (305 p), 10.2172/5415329, 1988.
991 Wood, R.: Stratocumulus Clouds, Monthly Weather Review, 140, 2373-2423,
992 10.1175/mwr-d-11-00121.1, 2012.
993 Wood, R., Wyant, M., Bretherton, C. S., Rémillard, J., Kollias, P., Fletcher, J., Stemmler, J.,
994 de Szoeke, S., Yuter, S., Miller, M., Mechem, D., Tselioudis, G., Chiu, J. C., Mann, J. A. L.,
995 O'Connor, E. J., Hogan, R. J., Dong, X., Miller, M., Ghate, V., Jefferson, A., Min, Q., Minnis,
996 P., Palikonda, R., Albrecht, B., Luke, E., Hannay, C., and Lin, Y.: Clouds, Aerosols, and
997 Precipitation in the Marine Boundary Layer: An Arm Mobile Facility Deployment, Bulletin of

998   the American Meteorological Society, 96, 419-440, https://doi.org/10.1175/BAMS-D-13-
999   00180.1, 2015.
1000  Zaveri, R. A., Barnard, J. C., Easter, R. C., Riemer, N., and West, M.: Particle-resolved
1001  simulation of aerosol size, composition, mixing state, and the associated optical and cloud
1002  condensation nuclei activation properties in an evolving urban plume, Journal of
1003  Geophysical Research: Atmospheres, 115, https://doi.org/10.1029/2009JD013616, 2010.
1004  Zhang, H., DeNero, S. P., Joe, D. K., Lee, H. H., Chen, S. H., Michalakes, J., and Kleeman,
1005  M. J.: Development of a source oriented version of the WRF/Chem model and its
1006  application to the California regional PM$_{10}$ / PM$_{2.5}$ air quality
1007  study, Atmos. Chem. Phys., 14, 485-503, 10.5194/acp-14-485-2014, 2014.
1008  Zhang, Z., Song, Q., Mechem, D. B., Larson, V. E., Wang, J., Liu, Y., Witte, M. K., Dong, X.,
1009  and Wu, P.: Vertical dependence of horizontal variation of cloud microphysics:
1010  observations from the ACE-ENA field campaign and implications for warm-rain simulation
1011  in climate models, Atmos. Chem. Phys., 21, 3103-3121, 10.5194/acp-21-3103-2021, 2021.
1012  Zheng, Q. and Miller, M. A.: Summertime Marine Boundary Layer Cloud, Thermodynamic,
1013  and Drizzle Morphology over the Eastern North Atlantic: A Four-Year Study, Journal of
1014  Climate, 35, 4805-4825, https://doi.org/10.1175/JCLI-D-21-0568.1, 2022.
1015  Zheng, X., Dong, X., Xi, B., Logan, T., and Wang, Y.: Distinctive aerosol-cloud-precipitation
1016  interactions in marine boundary layer clouds from the ACE-ENA and SOCRATES aircraft
1017  field campaigns, EGUsphere, 2023, 1-45, 10.5194/egusphere-2023-2608, 2023.
1018  Zheng, X., Xi, B., Dong, X., Wu, P., Logan, T., and Wang, Y.: Environmental effects on
1019  aerosol–cloud interaction in non-precipitating marine boundary layer (MBL) clouds over
1020  the eastern North Atlantic, Atmos. Chem. Phys., 22, 335-354, 10.5194/acp-22-335-2022,
1021  2022.
1022  Zheng, X., Qiu, S., Zhang, D., Adebiyi, A. A., Zheng, X., Faruque, O., Tao, C., and Wang, J.:
1023  Variability of Eastern North Atlantic Summertime Marine Boundary Layer Clouds and
1024  Aerosols Across Different Synoptic Regimes Identified with Multiple Conditions, ESS Open
1025  Archive, 10.22541/essoar.172434363.30466798/v1, 2024.
1026  Zheng, Y., Zhu, Y., Rosenfeld, D., and Li, Z.: Climatology of Cloud-Top Radiative Cooling in
1027  Marine Shallow Clouds, Geophysical Research Letters, 48, e2021GL094676,
1028  https://doi.org/10.1029/2021GL094676, 2021.
1029  Zhou, X. and Feingold, G.: Impacts of Mesoscale Cloud Organization on Aerosol-Induced
1030  Cloud Water Adjustment and Cloud Brightness, Geophysical Research Letters, 50,
1031  e2023GL103417, https://doi.org/10.1029/2023GL103417, 2023.

1032

1033

1034

1035

1036             Table 1. WRF physics scheme configuration

1037

| Physics Processes | Scheme | Reference |
|---|---|---|
| Microphysics | Morrison (2 moments) scheme | Morrison et al. (2009) |
| Longwave radiation | RRTMG scheme | Mlawer et al. (1997) |
| Shortwave radiation | RRTMG scheme | Iacono et al. (2008) |
| Surface-layer | Monin-Obukhov surface layer | Monin and Obukhov (1954) |
| Land surface | Unified Noah land-surface model | Chen and Dudhia (2001) |
| Planetary boundary layer | MYJ (Eta) TKE scheme (d01 and d02 only) | Mellor and Yamada (1982) Janjić (1994) |
| Shallow cumulus parameterization | GRIMS scheme (d01 and d02 only) | Hong and Jang (2018) |

1038

1039

1040

1041  Table 2. Ten-minute mean and standard deviation of cloud condensation nuclei (CCN), liquid
1042  water path (LWP), cloud droplet number (Nc), cloud radius (Re), and rainfall intensity (RI) over
1043  three study cases. Data are averaged over ~25 km of the domain 4 and total 16 averaged grids are
1044  in the domain 4. Rain and non-rain are averaged the grids when the RI on the grid is larger than
1045  and equal to zero, respectively. Only CCN are averaged within 1000 m height over the domain 4,
1046  other variables are averaged within 2000 m height.

| Area | Case | CCN (cm⁻³) | LWP (g m⁻²) | Nc (cm⁻³) | Re (μm) | RI (mm hr⁻¹) |
|---|---|---|---|---|---|---|
| Domain | Control | $73.07 \pm 48.77$ | $53.17 \pm 32.65$ | $22.68 \pm 11.59$ | $9.97 \pm 2.31$ | $0.009 \pm 0.033$ |
| | Perturbed | $286.88 \pm 183.69$ (+293%) | $79.25 \pm 56.62$ (+49%) | $59.74 \pm 27.29$ (+163%) | $7.83 \pm 2.02$ (-21%) | $0.008 \pm 0.033$ (-11%) |
| Rain | Control | $68.15 \pm 48.05$ | $58.57 \pm 31.69$ | $20.17 \pm 9.33$ | $10.47 \pm 2.07$ | $0.011 \pm 0.035$ |
| | Perturbed | $250.14 \pm 153.23$ (+267%) | $91.81 \pm 55.06$ (+57%) | $53.01 \pm 20.39$ (+163%) | $8.35 \pm 1.83$ (-20%) | $0.009 \pm 0.036$ (-18%) |
| Non-Rain | Control | $103.73 \pm 41.52$ | $18.91 \pm 9.81$ | $38.57 \pm 11.93$ | $6.81 \pm 0.76$ | $0 \pm 0$ |
| | Perturbed | $444.47 \pm 217.08$ (+328%) | $24.22 \pm 15.80$ (+28%) | $89.24 \pm 33.42$ (+131%) | $5.54 \pm 0.90$ (-19%) | $0 \pm 0$ |

1047
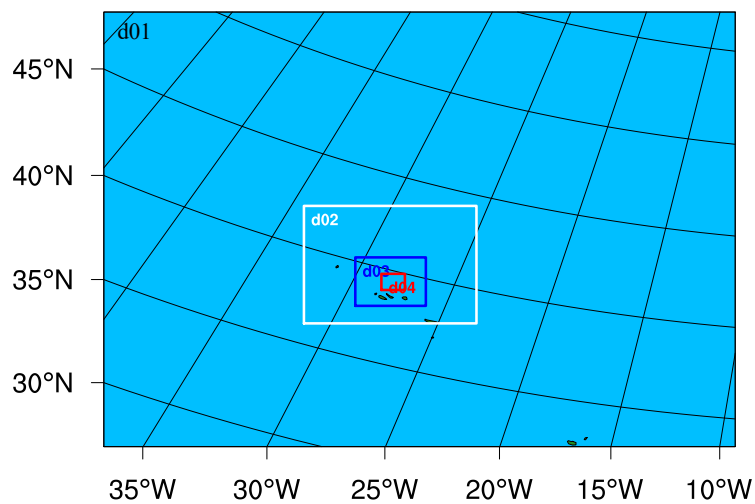
1048

Figure 1. Model domains are designed for simulations. The 4 domains with 4 horizontal
resolution of 5 km (d01), 1.67 km (d02), 0.56 km (d03), and 0.19 km (d04), respectively.

1051

1052
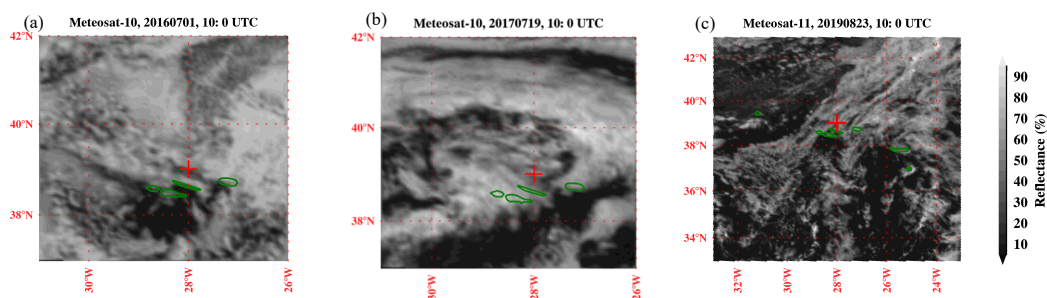


1053
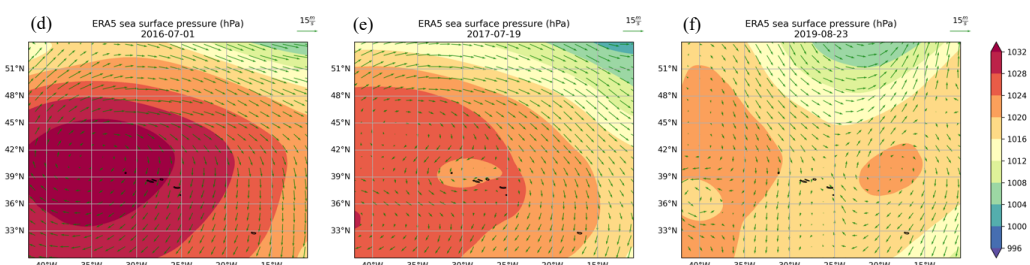


1054
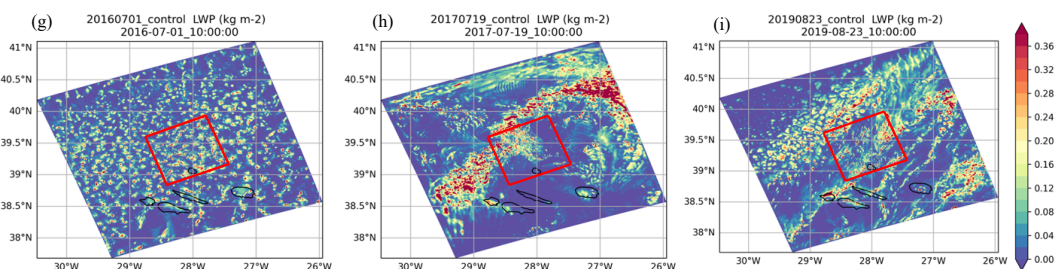


1055

Figure 2. Spinning Enhanced Visible Infra-Red Imager (SEVIRI) images from Meteosat satellite
at 10:00 UTC on (a) 1 July 2016, (b) 19 July 2017, and (c) 23 August 2019 over the ENA. (d),
(e), and (f) are on the same day of (a), (b), and (c), respectively, but they are from ERA5 mean
sea surface pressure (contour; units: hPa) and 10-meter surface wind (arrow; units: m s$^{-1}$). (g),
(h), and (i) are on the same day of (a), (b), and (c), respectively, but they are WRF-Chem
simulated liquid water path (LWP; units: kg m$^{-2}$) in the control runs. The red boxes in the figures
indicate the result from the domain 4.

1063

1064

1065

1066
1067

Figure 3. The time series of temperature profiles (units: K) from ARM interpolated soundings at
the Azores (39.09°N, -28.02°W) on (a) 1 July 2016, (c) 19 July 2017, and (e) 23 August 2019.
Panels (b), (d), and (f) depict the same dates as (a), (c), and (e), respectively, but show the
average temperature from WRF-Chem simulated results over 20 × 20 grids centered on the
Azores (approximately 4 km resolution).
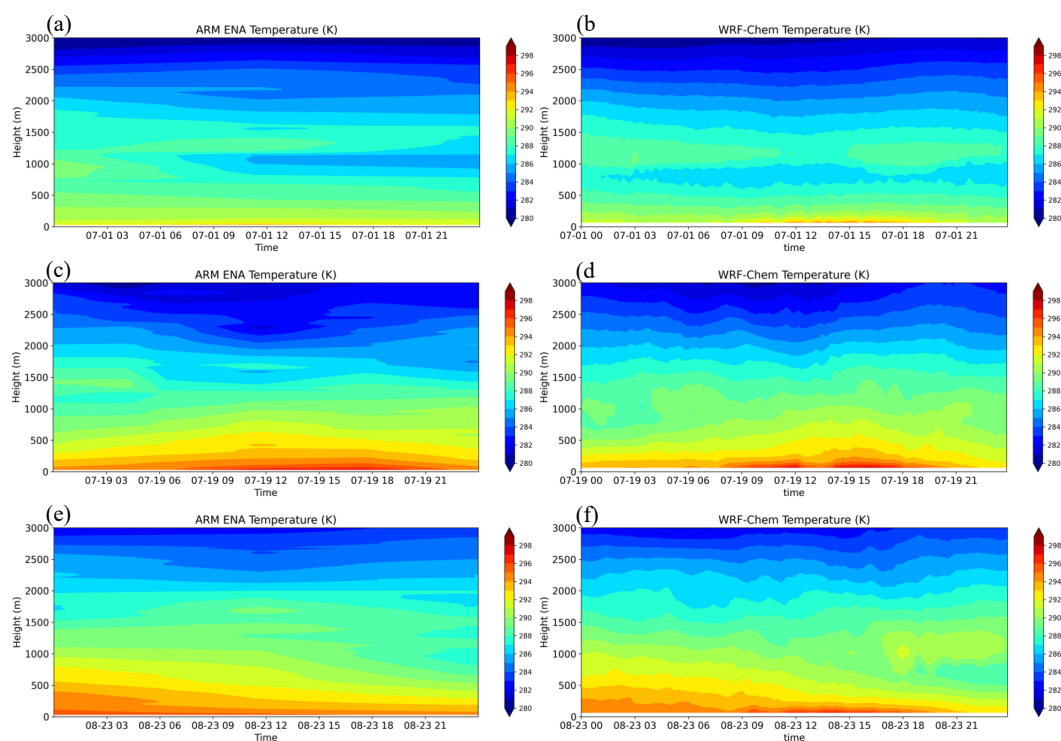
1068
1069
1070
1071
1072
1073
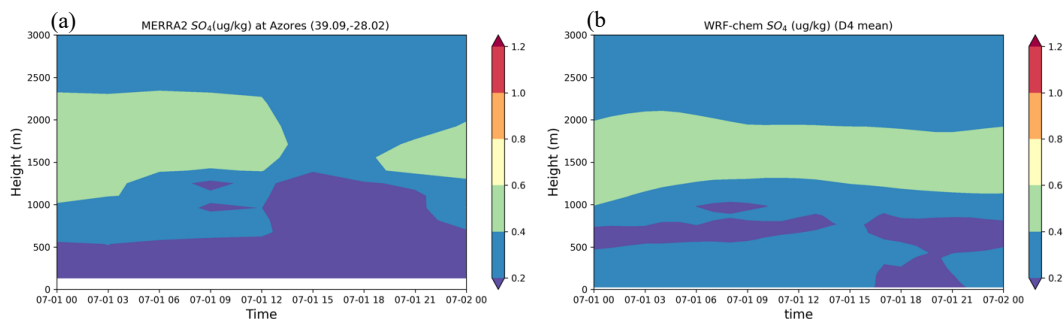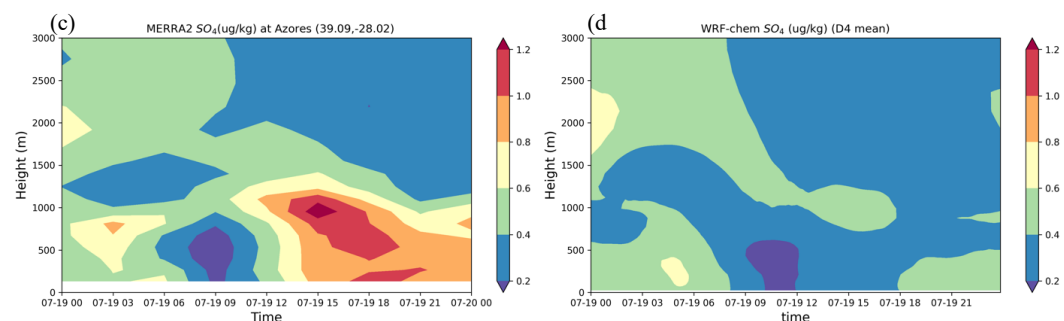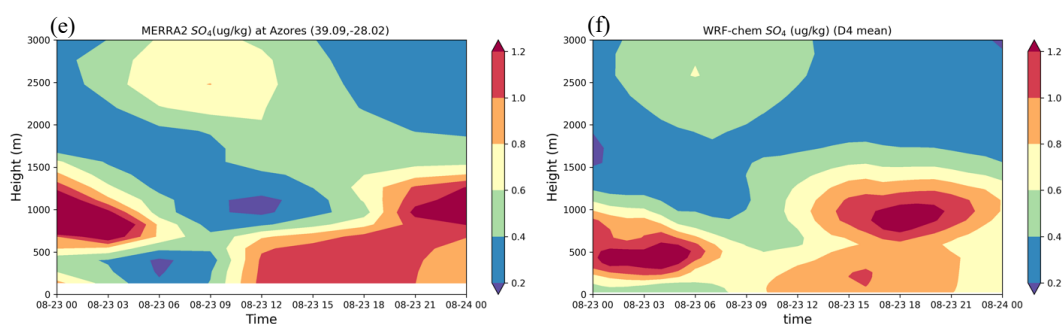
Figure 4. The time series of SO₄ profiles (units: µg kg⁻¹) from MERRA-2 at the Azores (39.09°N, -28.02°W) on (a) 1 July 2016, (c) 19 July 2017, and (e) 23 August 2019. Panels (b), (d), and (f) depict the same dates as (a), (c), and (e), respectively, but show the average aerosol concentration from WRF-Chem simulated data over the domain 4.

1082
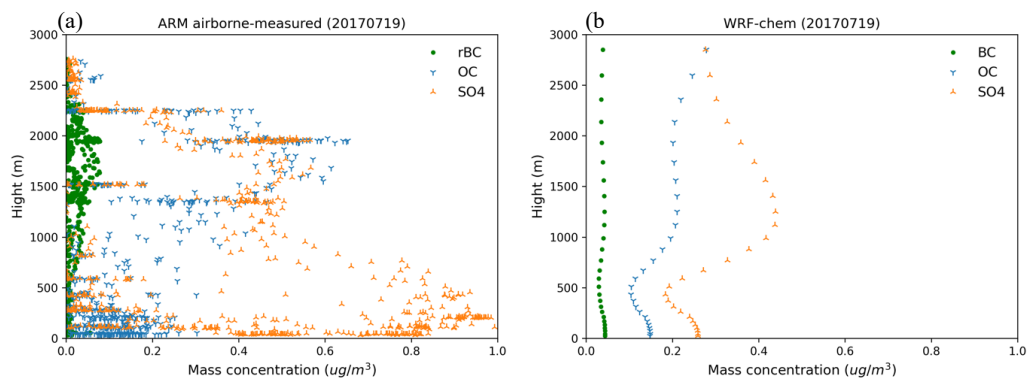


1083
1084
1085    Figure 5. (a) ARM airborne-measured vertical profiles of SO$_4$, OC and refractory BC (rBC) mass
1086    concentration (units: μg cm$^{-3}$) averaged over multiple flights on 19 July 2017. Noted that the
1087    highly uncertain and noisy aerosol observations between 600 – 1000 m height due to cloud
1088    contamination. (b) WRF-Chem simulated vertical profile of SO$_4$, OC and BC mass concentration
1089    (units: μg cm$^{-3}$) averaged over the domain 4 during the flight time from 8:40 to 11:50 UTC.
1090
1091
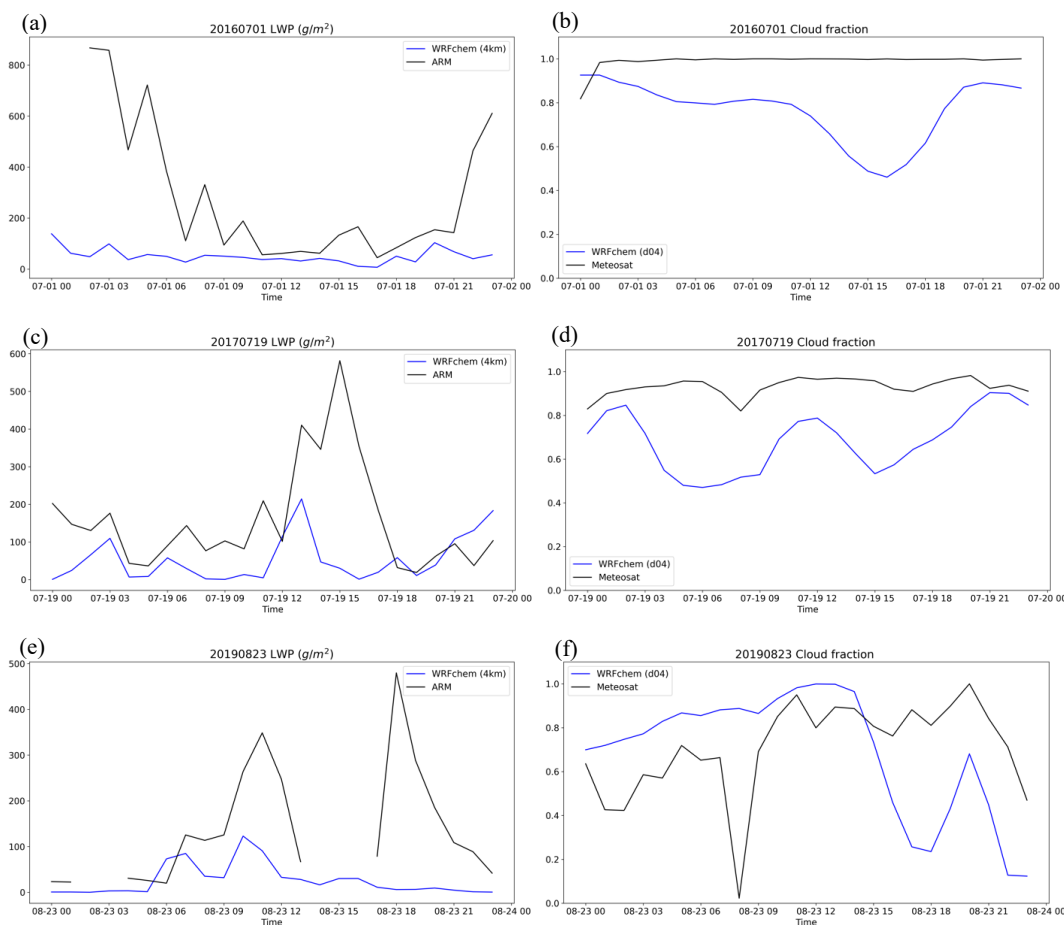
1092

1093

1094
1095
1096 Figure 6. (a), (c), and (e) are the hourly time series of 4 km-averaged (4km) liquid water path
1097 (units: g m$^{-2}$) simulated from WRF-Chem (blue solid line) and observaed from ARM (black solid
1098 line) on 1 July 2016, 19 July 2017, and 23 August 2019, respectively. (b), (d), and (f) are the
1099 hourly time series of domain-averaged (d04) cloud fraction simulated from WRF-Chem (blue
1100 solid line) and observaed from Meteosat (black solid line) on 1 July 2016, 19 July 2017, and 23
1101 August 2019, respectively. The 4 km-averaged data are averaged from the model simulated
1102 results over 20 × 20 grids centered on the Azores (approximately 4 km resolution).

1103

1104
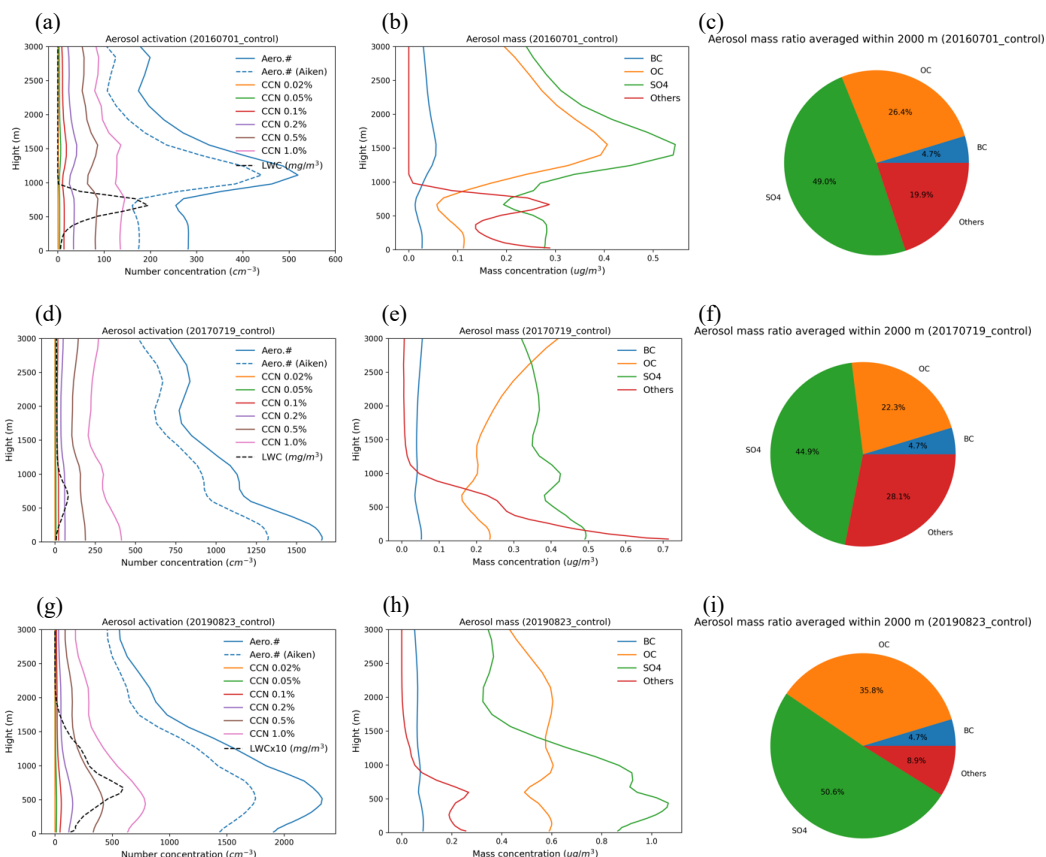
Figure 7. (a), (d), and (g) WRF-Chem vertical profiles of aerosol number concentration (Aiken mode and accumulation mode; units: cm$^{-3}$), aerosol number concentration (Aiken mode only; units: cm$^{-3}$), CCN number concentration under different supersaturations (units: cm$^{-3}$), and liquid water content (cloud and rain; units: mg m$^{-3}$) averaged over the domain 4 on 1 July 2016, 19 July 2017, and 23 August 2019, respectively, in the control runs. (b), (e), and (h) WRF-Chem vertical profiles of BC, OC, SO$_4$, and other species (like sea salts) (units: µg cm$^{-3}$) averaged over the domain 4 on 1 July 2016, 19 July 2017, and 23 August 2019, respectively, in the control runs. (c), (f), and (i) Pie chart of aerosol mass of different species averaged within 2000 m height on 1 July 2016, 19 July 2017, and 23 August 2019, respectively, in the control runs. Note that LWC quantity is adjusted to fit the scale of x-axis for each case.

(a)


(b)


1124

(c)


(d)


1125

(e)


(f)
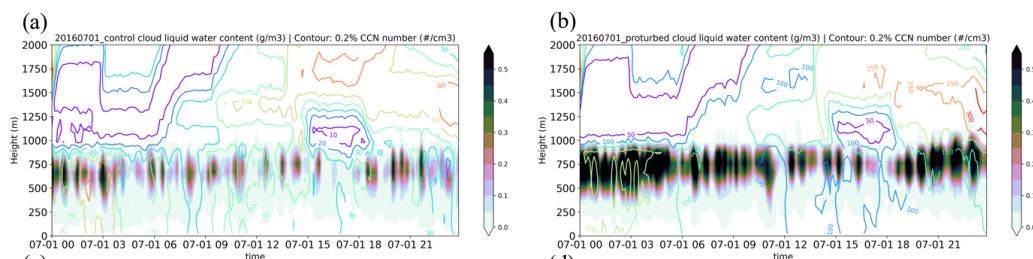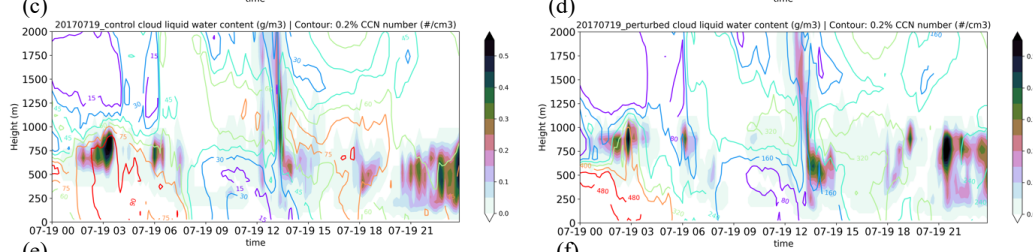

1126
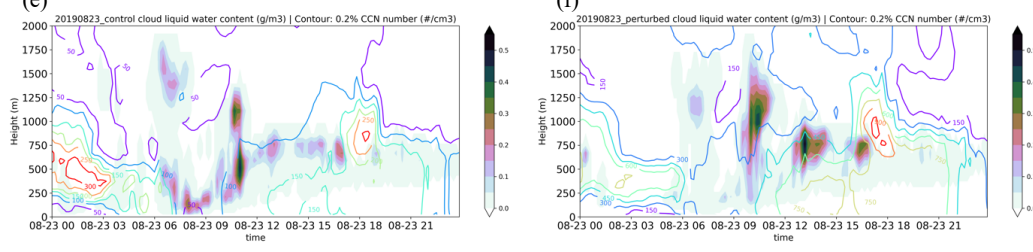
1127 Figure 8. (a), (c), and (e) are the time series of 4 km-averaged cloud liquid water content profile
1128 (shade; units: g cm$^{-3}$) and CCN (0.2% supersaturation) number concentration profile (contour;
1129 units: # cm$^{-3}$) on 1 July 2016, 19 July 2017, and 23 August 2019, respectively, in the control
1130 runs. (b), (d), and (f) are the same as (a), (c), and (e), respectively, but in the perturbed runs. The
1131 data are averaged from the model simulated results over 20 × 20 grids centered on the Azores
1132 (approximately 4 km resolution).
1133

1134

1135
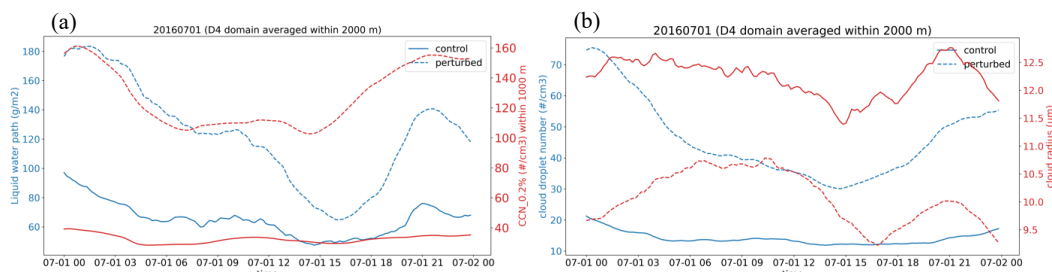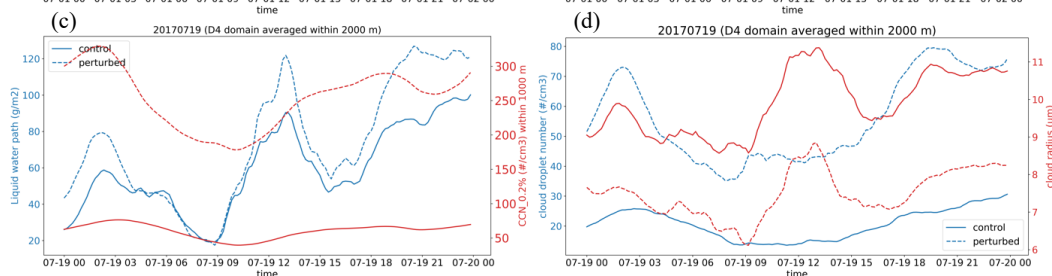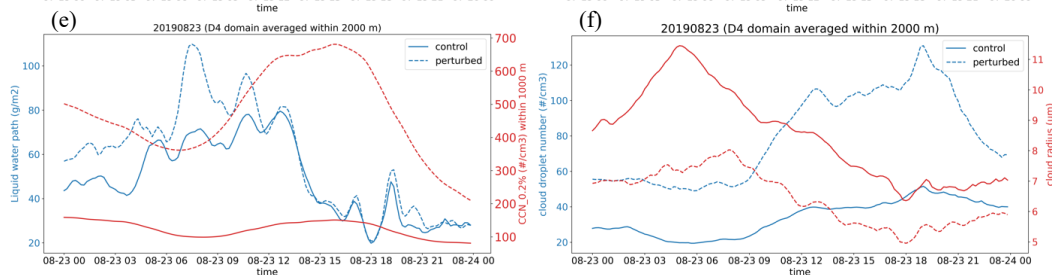
Figure 9. (a), (c), and (e) are the time series of domain-averaged liquid water path (blue lines; units: g m$^{-2}$) and CCN number concentration under 0.2% supersaturation (red lines; units: # cm$^{-2}$) for the control case (soild lines) and the perturbed case (dashed lines) on 1 July 2016, 19 July 2017, and 23 August 2019, respectively. (b), (d), and (f) are the time series of domain-averaged cloud droplet number (blue lines; units: # cm$^{-3}$) and cloud radius (red lines; units: μm) for the control (soild lines) and perturbed (dashed lines) on 1 July 2016, 19 July 2017, and 23 August 2019, respectively. Only CCN data are averaged within 1000 m height over the domain 4, other variables are averaged within 2000 m height.
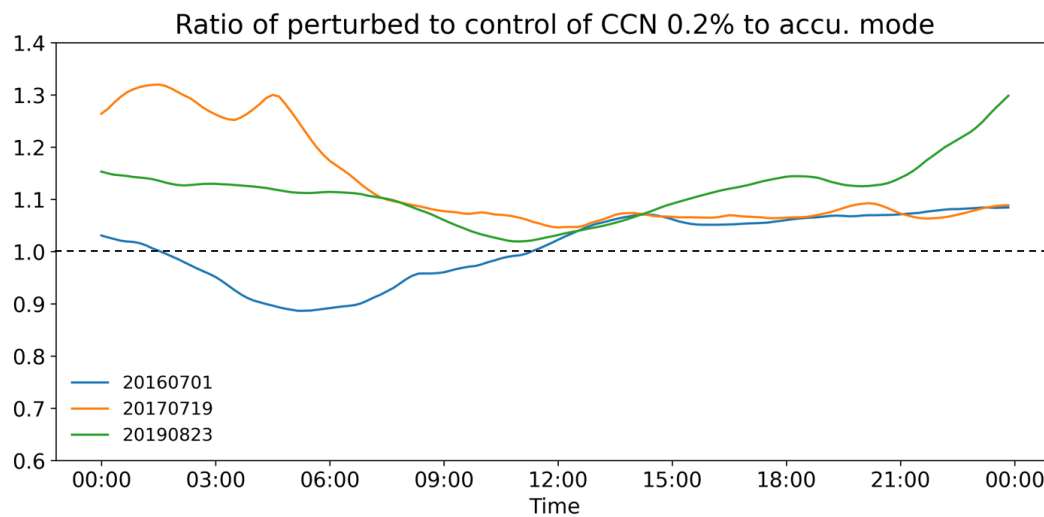
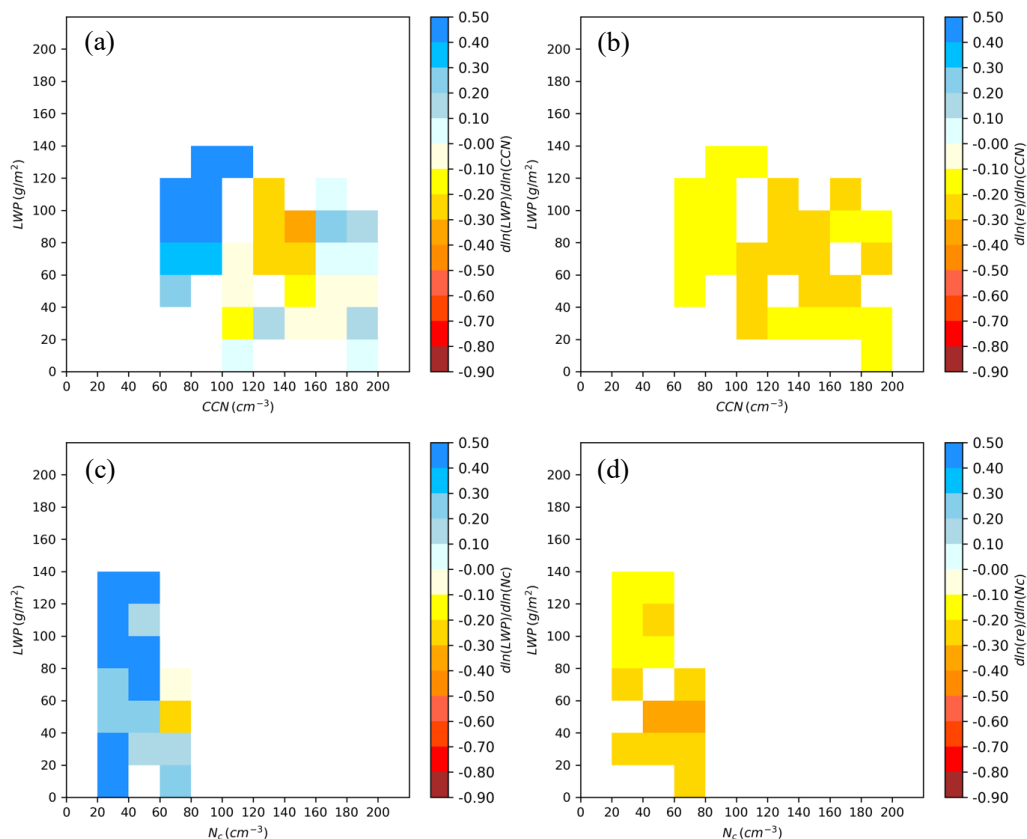Figure 10. The time series of ratio of the precentage of activated CCN at 0.2% supersaturation to perturbed to the accumulation mode aerosols between perturbed and control runs. The back dashed line indicates the value of 1.0.

Figure 11. (a) and (b) are the mean liquid water path (LWP) and cloud radius (Re) susceptibilities for different cloud condensation nuclei (CCN) and LWP bins for three study cases, respectively. (c) and (d) are the same as (a) and (b), respectively, but for different cloud droplet number (Nc) and LWP bins. The logarithmic slope between LWP and CCN, denoted as $(dln(LWP)/dln(CCN))$, is calculated at each output time (every 10 minutes) using data from 16 aggregate grid points (~25 km for each grid point) from the control run and 16 aggregated grid points from the perturbed run.

1165
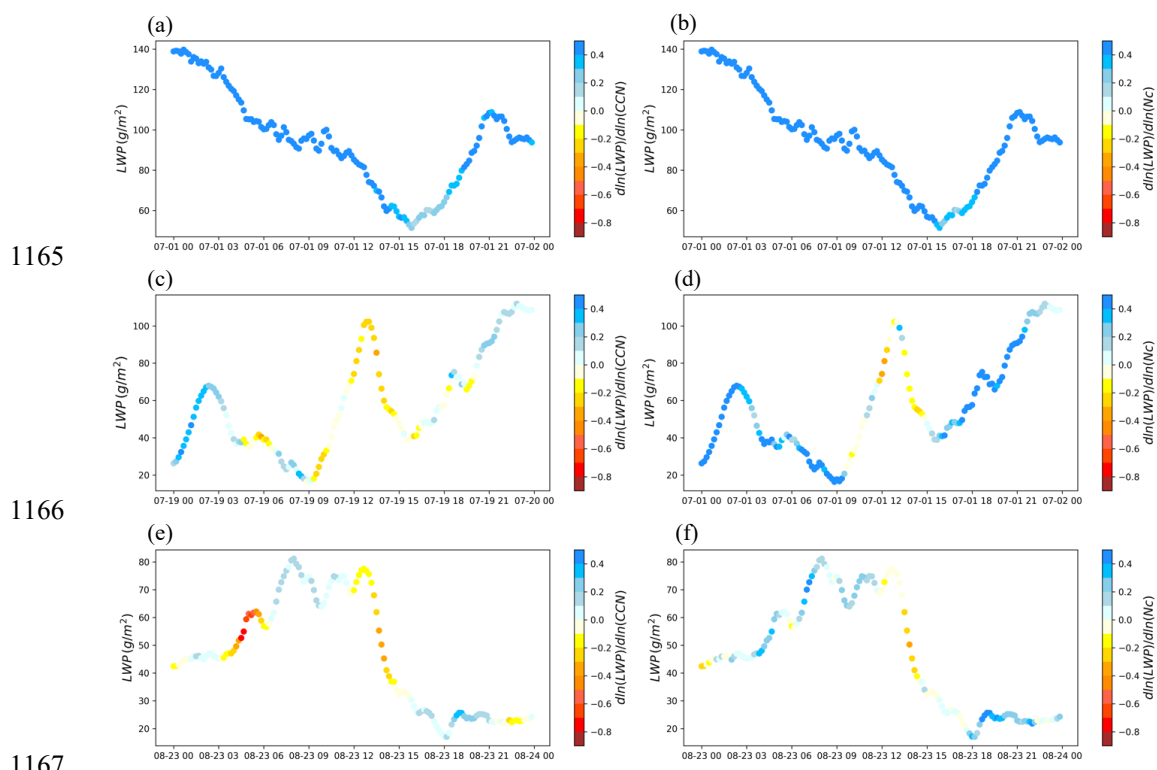


1166

1167

Figure 12. (a), (c) and (e) are the time variable of LWP susceptibility for different CCN
concentration, denoted as ($dln(LWP)/dln(CCN)$), on 1 July 2016, 19 July 2017, and 23 August
2019, respectively. (b), (d) and (f) are the time variable of LWP susceptibility for different Nc
concentration, denoted as ($dln(LWP)/dln(Nc)$), on 1 July 2016, 19 July 2017, and 23 August
2019, respectively. The logarithmic slope between LWP and CCN is calculated at each output
time (every 10 minutes) using data from 16 aggregate grid points (~25 km for each grid point)
from the control run and 16 aggregated grid points from the perturbed run.

1175
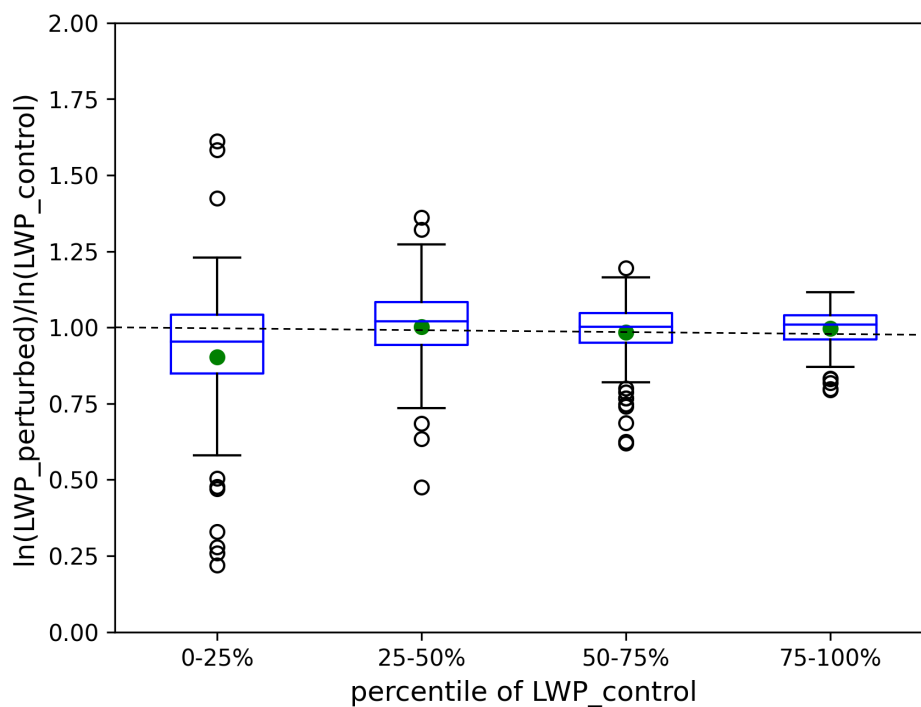
Figure 13. The boxplot of the relative change in $ln(LWP)$ between the perturbed and control cases across different LWP percentile rages in the control case during the negative susceptibility for LWP shown in Fig. 12. The box extends from the first quartile to the third quartile of the data, with a line at the median. The whiskers extend from the box to the farthest data point lying within 1.5x the inter-quartile range from the box. Flier points are those past the end of the whiskers. Green dots are the mean value, and the back dashed line indicates the value of 1.0.